IEEE Access
Multidisciplinary | Rapid Review | Open Access Journal

Received January 5, 2019, accepted February 13, 2019, date of publication March 4, 2019, date of current version March 25, 2019.

Digital Object Identifier 10.1109/ACCESS.2019.2902859

Near-Field MIMO-SAR Millimeter-Wave Imaging With Sparsely Sampled Aperture Data

MUHAMMET EMIN YANIK, (Student Member, IEEE), AND MURAT TORLAK, (Senior Member, IEEE)

Department of Electrical and Computer Engineering, The University of Texas at Dallas, Richardson, TX 75080, USA

Corresponding author: Muhammet Emin Yanik (muhammet.yanik@utdallas.edu)

This work was supported by the Semiconductor Research Corporation (SRC) task 2712.029 through The University of Texas at Dallas' Texas Analog Center of Excellence (TxACE).

ABSTRACT The primary challenge of a cost-effective and low-complexity near-field millimeter-wave (mmWave) imaging system is to achieve high resolution with a few antenna elements as possible. Multiple-input multiple-output (MIMO) radar using simultaneous operation of spatially diverse transmit and receive antennas is a good candidate to increase the number of available degrees of freedom. On the other hand, higher integration complexity of extremely dense transceiver electronics limits the use of MIMO only solutions within a relatively large imaging aperture. Hybrid concepts combining synthetic aperture radar (SAR) techniques and sparse MIMO arrays present a good compromise to achieve short data acquisition time and low complexity. However, compared with conventional monostatic sampling schemes, image reconstruction methods for MIMO-SAR are more complicated. In this paper, we propose a high-resolution mmWave imaging system combining 2-D MIMO arrays with SAR, along with a novel Fourier-based image reconstruction algorithm using sparsely sampled aperture data. The proposed algorithm is verified by both simulation and processing real data collected with our mmWave imager prototype utilizing commercially available 77-GHz MIMO radar sensors. The experimental results confirm that our complete solution presents a strong potential in high-resolution imaging with a significantly reduced number of antenna elements.

INDEX TERMS Millimeter-wave radar (mmWave), near-field radar imaging, synthetic aperture radar (SAR), frequency-modulated continuous-wave (FMCW), multiple-input multiple-output (MIMO) radar, IWR1443 mmWave sensors.

I. INTRODUCTION

Millimeter-wave (mmWave) imaging technology has gained significant attention in recent years and it now plays an important role in many applications including medical diagnostics [1]–[3], security screening [4]–[9], and structure inspection [10]. The major challenges of building mmWave imaging systems are the cost and complexity arising from the need for a large number of transceiver elements.

The cross-range image resolution and the spatial sampling criteria are two key system parameters that determine the required number of antennas. While the range resolution is directly related to the bandwidth of the transmitting signal, the cross-range resolution is also determined by the effective length of the radar aperture. For example, an effective aperture size of 50 wavelengths (λ) along both horizontal and vertical directions is needed to achieve a 5 mm resolution in both axes at 50 cm range [4], [5]. On the other hand, $\lambda/4$ spacing is necessary between the measurement points to prevent the formation of unwanted imaging artifacts in a near-field scenario [4]. Hence, in order to satisfy the above mentioned image resolution under the required spatial sampling criteria, an ideal imaging system would consist of a two-dimensional (2-D) array with approximately 40000 antenna elements.

In recent years, great progress has been made in the semiconductor technology to enable cost-effective sensor solutions. Complementary metal-oxide semiconductor (CMOS) based frequency-modulated continuous-wave (FMCW) mmWave radars integrate all the analog and radio-frequency (RF) functionality as well as the low-level signal processing capability into a single chip with a compact form factor [11]. Such a highly integrated device enables the

The associate editor coordinating the review of this manuscript and approving it for publication was Lin Wang.

mmWave radar systems to be cost-effective and miniaturized. However, implementing densely placed transceivers required for high-resolution imaging is still a challenging effort.

A well-known approach to mitigate this challenge is the realization of multiple-input multiple-output (MIMO) array topologies [12]–[14]. Fully electronic multistatic sampling of large radar apertures using MIMO arrays has been incorporated into various near-field imaging systems [6], [15], [16]. While real-time operation is an ultimate goal for many applications, higher hardware complexity of integrating a large number of transceiver antennas makes fully electronic sampling less likely to be widely deployed. As a result, using a hybrid concept based on the combination of synthetic aperture radar (SAR) technique [17], [18] and MIMO array leads to lower hardware complexity than fully electronic sampling solutions [5], [19]. On the other hand, employing computationally efficient image reconstruction algorithms remains a challenge for MIMO-SAR configurations, especially in near-field imaging applications.

In near-field, the plane-wave assumption is invalid and the spherical electromagnetic wave model has to be used. The image reconstruction process must be able to completely compensate for the curvature of the wavefront. Although the time-domain correlation (or backprojection) method [5], [20], which provides a straightforward solution to estimate target area reflectivity by correlating the recorded data with the signature of a unit reflector at each spatial coordinate, can be used for any arbitrary multistatic array configuration, it suffers from high computational load.

For monostatic sampling schemes, where the measurements are taken by collocated transmit and receive antennas over regular spatial intervals, near-field image reconstruction has long been implemented using Fourier based inversion methods for both planar [4], [21], [22] and cylindrical/spherical [23], [24] scanning geometries. Unfortunately, these methods cannot be directly used for multistatic systems due to their need to consider the different trajectories of the incident and reflected electric fields.

Modified wavenumber domain image reconstruction algorithms accounting for multistatic array topology along with wavefront curvature in near-field have been presented for 2-D planar MIMO arrays [25], and for the systems synthesizing the 2-D aperture with one-dimensional (1-D) SAR along with 1-D MIMO sampling [19]. However, these techniques require uniform spatial sampling and involve computationally expensive wavenumber space interpolation. Hence, such needs limit the use of these algorithms for arbitrary array configurations and make them equally or less efficient than the direct time-domain reconstruction [5] in high throughput applications.

In response to all these major challenging requirements, we propose a novel near-field mmWave imaging solution that combines 2-D sparse MIMO arrays and SAR. We investigate the wavenumber domain of the backscattered data by expanding the study in [26] for SAR configuration. We establish the nonlinear relation between the wavenumber spectrum of the backscattered data and the reconstructed image, which, to our knowledge, has not been studied in the previous literature. We analyze the analytical effect of aliasing due to sparse sampling both on the wavenumber and spatial domains. We then propose an efficient Fourier based imaging algorithm for sparse MIMO-SAR to recover the spectrum of alias-free images by properly combining the overlapped spectrum of sparse subchannels.

The proposed image reconstruction algorithm for sparse multistatic sampling is based on the expansion of extremely efficient and interpolation-free Fourier based monostatic SAR imaging. To reconstruct near-field images from spatially diverse transmit and receive antennas, we introduce a multistatic-to-monostatic phase correction approach. In addition, the proposed reconstruction formula compensates the propagation loss, which is typically ignored in existing studies, to improve the imaging quality for the near-field operations.

To demonstrate the effect of sparse sampling and to validate the proposed image reconstruction algorithm, we build a mmWave imaging prototype utilizing commercially available MIMO sensors and a custom designed two-axis automatic rail system. We investigate key system parameters such as image resolution and spatial sampling criteria. We implement a calibration method to compensate the gain and phase mismatches of the MIMO array elements [27], [28]. We present real imaging results to show the effectiveness of proposed system that achieves high-resolution imaging performance with a significantly reduced number of antenna elements.

The rest of the paper is organized as follows. Section II presents the proposed MIMO-SAR configuration, and discusses the virtual antenna array concept in near-field using a multistatic-to-monostatic correction factor to improve Fourier based image formation. Section III reviews the standard monostatic SAR image reconstruction framework, which forms the basis of our MIMO-SAR image formation. Section IV addresses the signal processing steps involved in the proposed sparse MIMO-SAR image reconstruction starting with the wavenumber spectrum analysis of subsampling and its effect on the image domain, followed by the proposed novel image reconstruction technique that is compatible with the sparsely sampled aperture data. Section V discusses the image resolution, which is an important performance metric in imaging. Section VI presents the hardware architecture of the prototyped imager and MIMO array calibration. Simulations and measurement results are reported in Section VII, which is followed by conclusions.

II. SYSTEM MODEL

In this paper, we propose to synthesize a 2-D SAR aperture by mechanically scanning a MIMO array in a parallel track pattern as shown in Fig. 1. In the following subsections, we present the geometrical setup for the proposed MIMO-SAR system.

A. MIMO-SAR CONFIGURATION

The radar measurements are performed by moving a MIMO array continuously across xy plane, along parallel lines, as shown in Fig. 1. Both SAR and MIMO apertures can be sparse. The unprimed and primed coordinates represent the measurement positions on the scan aperture and image pixel positions over a target aperture, respectively. In the established right-handed (x, y, z) Cartesian coordinate system, $x-$axis, $y-$axis, and $z-$axis denote horizontal, vertical, and depth directions, respectively.

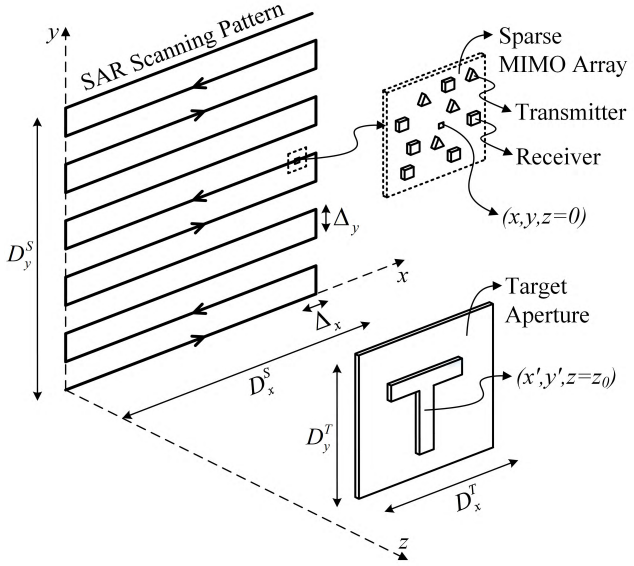

FIGURE 1. Geometry of SAR scanned in a parallel track pattern with a sparse MIMO array.

The reference point $(x, y, 0)$ is the position of the MIMO array at a specific measurement instant. The target aperture is at the distance of z_0. The image pixel coordinates are given as (x', y', z_0). In this paper, the target is assumed to be a 2-D object and parallel to the scanning plane. We will report our 3-D image formation results in a future article.

B. THE VIRTUAL ARRAY CONCEPT

We consider a sparse MIMO array equipped with M_T transmit and M_R receive antenna elements. Let the uth transmit and the vth receive antennas be located at $\mathbf{r}_u \in \mathbb{R}^3$ and $\mathbf{r}_v \in \mathbb{R}^3$, respectively, as shown in Fig. 2a. The transmit and receive antenna locations are characterized by

$$g_T(\mathbf{r}) = \sum_{u=0}^{M_T-1} \delta(\mathbf{r}-\mathbf{r}_u), \qquad g_R(\mathbf{r}) = \sum_{v=0}^{M_R-1} \delta(\mathbf{r}-\mathbf{r}_v). \quad (1)$$

In a far-field scenario, assume that the distance to the target aperture is much larger than the distance between the transmit and receive elements of the MIMO array. This assumption leads to a conventional midpoint approximation that holds for a small fraction of ϵ for each $u \in \{1, \ldots, M_T\}$ and $v \in \{1, \ldots, M_R\}$ as reported in [29],

$$|\mathbf{r}_u - \mathbf{r}_v| \leq \sqrt{4\epsilon\lambda R}, \quad (2)$$

where λ is the wavelength and R is the distance from the midpoint of the antennas to the ideal point scatterer. Then the corresponding transceiver antenna pair is approximated by a single monostatic virtual element located at [13], [29], [30]

$$\mathbf{r}_{uv} = (\mathbf{r}_u + \mathbf{r}_v)/2. \quad (3)$$

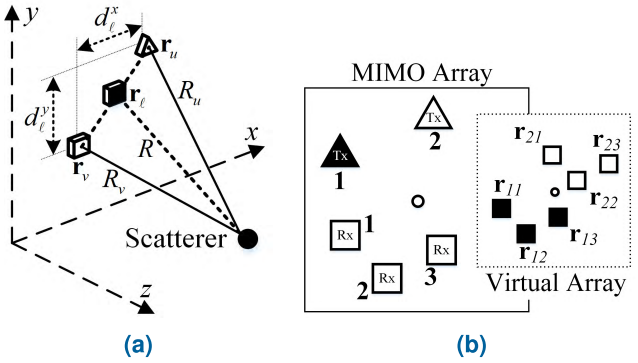

FIGURE 2. (a) MIMO array in near-field for uth transmit and vth receive antennas. (b) An example of MIMO array with two transmit and three receive antennas, and corresponding virtual array.

The scaling factor of $1/2$ is due to the round-trip propagation. The location of this monostatic virtual element as depicted in Fig. 2a is also called equivalent phase center. An example of MIMO array with $M_T = 2$ and $M_R = 3$ antennas and the corresponding virtual array are depicted in Fig. 2b. Thus, a MIMO array with $M_T + M_R$ physical antennas can be approximated by a virtual array with $L = M_T \times M_R$ monostatic elements. We can simplify the virtual element subscript as ℓ, where $\ell \in \{1, \ldots, L\}$, for simplicity. Then the corresponding distribution function of the virtual array elements can be obtained by performing convolution of the transmitter and receiver element distributions in (1) as

$$g_V(\mathbf{r}) = g_T(\mathbf{r}) \circledast g_R(\mathbf{r}) = \sum_{\ell=0}^{L-1} \delta(\mathbf{r}-\mathbf{r}_\ell). \quad (4)$$

Therefore, the virtual array, which describes the set of independent monostatic elements that can collect the equivalent data, is half the size of the physical MIMO array (i.e., sum of the transmit and receive array aperture sizes) in each dimension. To create this virtual array architecture, receiver antennas must be able to separate the signals corresponding to different transmitter antennas. In this paper, the orthogonality between the transmit antennas is achieved by employing time division multiplexing (TDM) technique.

C. THE VIRTUAL ARRAY RESPONSE IN NEAR-FIELD IMAGING

For near-field imaging applications, small fraction of ϵ assumption in (2) does not hold and an improved approximation is necessary. In the following, we will derive an efficient

proper adjustment factor to create an equivalent virtual array from a MIMO array for near-field scenarios.

Let us express the total round-trip distance associated with the uth transmitter element at $(x_u, y_u, 0)$ and the vth receiver element at $(x_v, y_v, 0)$ to a point scatterer at (x', y', z_0) as

$$R_\ell = R_u + R_v = \sqrt{(x_u - x')^2 + (y_u - y')^2 + z_0^2} + \sqrt{(x_v - x')^2 + (y_v - y')^2 + z_0^2}. \quad (5)$$

Let us denote the location of the virtual antenna element corresponding to the uth transmitter and the vth receiver as (x, y). We can express the uth transmitter and the vth receiver locations as

$$\begin{aligned} x_u &= x + d_\ell^x/2, \quad y_u = y + d_\ell^y/2, \\ x_v &= x - d_\ell^x/2, \quad y_v = y - d_\ell^y/2, \end{aligned} \quad (6)$$

where d_ℓ^x and d_ℓ^y are the distances between the transmitter and receiver elements in x and y axes, respectively, as shown in Fig. 2a. Applying multivariate Taylor series expansion to (5) up to third order terms with respect to the parameters d_ℓ^x and d_ℓ^y around zero, as described in the Appendix C, we can obtain

$$R_\ell \approx 2R + \frac{(d_\ell^x)^2 + (d_\ell^y)^2}{4R} - \frac{((x - x')d_\ell^x + (y - y')d_\ell^y)^2}{4R^3}, \quad (7)$$

where

$$R = \sqrt{(x - x')^2 + (y - y')^2 + z_0^2}, \quad (8)$$

is the distance between the midpoint and the scatterer. Considering $(x - x'), (y - y') \ll z_0$ for the second order terms in (7), we can obtain an improved approximation to the total round-trip distance associated with the ℓth virtual element in terms of

$$R_\ell \approx 2R + \frac{(d_\ell^x)^2 + (d_\ell^y)^2}{4z_0}. \quad (9)$$

D. SIGNAL MODEL

In recent years, several mmWave sensors based on FMCW signaling have been successfully constructed especially targeting automotive radar applications. FMCW (also known as chirp waveform) offers several advantages, i.e., large signal bandwidth, range processing gain, the inherent isolation between transmitters and receivers, and low sampling rate. Based on the improved virtual antenna array concept presented in the previous section and TDM technique, the transmit and receive antennas are paired to approximate a monostatic radar operation. Thus, let us briefly review a single element monostatic radar signal model.

Consider an FMCW signal transmitted by the monostatic antenna element in complex form as

$$m(t) = e^{j2\pi(f_0 t + 0.5Kt^2)}, \quad 0 \le t \le T, \quad (10)$$

where f_0 is the carrier frequency at time $t = 0$, $K = B/T$ is the slope of frequency computed from the sweep bandwidth of B, and the chirp duration of T. Assuming an ideal point scatter at a distance of R, the received signal by the same monostatic antenna element is delayed and scaled version of the transmitted signal

$$\hat{s}(t) = \sigma m(t - \tau) = \sigma e^{j2\pi(f_0(t-\tau) + 0.5K(t-\tau)^2)}, \quad (11)$$

where $\tau = 2R/c$ is the round-trip delay of the echo for the target distance of R, c is the speed of light, and σ is the combination of target reflectivity and round-trip amplitude decay with range [25], [31]

$$\sigma = p/R^2, \quad (12)$$

where p is the complex reflectivity of the ideal point target. The radar demodulates the received signal by mixing it with a copy of the transmitted signal to reduce the required system sampling rate. This is known as dechirping and results in a complex intermediate frequency (or beat) signal [32]

$$s(t) = \sigma e^{j2\pi(f_0\tau + K\tau t - 0.5K\tau^2)}, \quad (13)$$

where $K\tau$ term is the beat frequency which carries the range information. The last term of (13) is known as the residual video phase (RVP), which is found to be negligible [33]. Therefore, the beat signal can be rewritten in the wavenumber domain as

$$s(k) = p\frac{e^{j2kR}}{R^2}, \quad \frac{2\pi f_0}{c} \le k \le \frac{2\pi f_T}{c}, \quad (14)$$

where $f_T = f_0 + KT$ is the maximum swap frequency of FMCW radar and $k = 2\pi f/c$ is the wavenumber corresponding to the frequency f.

Now we are ready to introduce the midpoint approximation derived in Section II-C. The approximation in (9) allows a MIMO array with sparsely placed transmit and receive elements to be converted to a virtual monostatic array more accurately for near-field imaging applications. The effectiveness of the image reconstruction is mainly determined by proper handling of the phase in (14), and any improvement in the amplitude decay with range will have little impact on the reconstructed image. Therefore, substituting (9) into the phase term in (14), we can express the received signal by the ℓth hypothetical monostatic virtual element as

$$s_\ell(k) \approx p\frac{e^{jkR_\ell}}{R^2} = s(k)e^{j\phi_\ell(k)}, \quad (15)$$

where $s(k)$ is the signal that would be received by a physical monostatic element located at the same midpoint between actual transmitter and receiver antennas, and

$$\phi_\ell(k) = k\frac{(d_\ell^x)^2 + (d_\ell^y)^2}{4z_0}, \quad (16)$$

is the nonlinear phase term as a result of the improved approximation in (9) needed for near-field applications.

In the MIMO-SAR imaging configuration, the acquired 3-D backscattered data cube $s_\ell(x, y, k)$ from the ℓth virtual channel is a function of two spatial coordinates, antenna pair spacing, target distance and the wavenumber. If the 2-D distributed target at z_0 is characterized by its complex reflectivity function $p(x', y')$, the main purpose of the

MIMO-SAR imaging algorithm is to recover $p(x', y')$ from the reflected signals $s_\ell(x, y, k)$ captured by all independent and arbitrary located virtual elements.

III. IMAGE RECONSTRUCTION WITH MONOSTATIC SAR

Here, we review the standard monostatic SAR image reconstruction framework [4], [21], which forms the basis of our proposed algorithms. We adopt the signal model that assumes continuously recorded aperture data. Based on this model, we will determine the important relationship between $k-$domain (or spectral domain) and image domain (or spatial domain) when the imaging aperture is sparsely sampled by MIMO-SAR in Fig. 1.

We assume the linearized scattering model with the target reflectivity of $p(x', y')$. By expanding the signal model in (14), we can express the received backscattered data from a planar target at a distance of z_0 as

$$s(x, y, k) = \iint p(x', y') \frac{e^{j2kR}}{R^2}\, dx'\, dy', \tag{17}$$

where R is the distance between the transceiver element and a general point on the target given in (8). We include the amplitude factor in the signal model due varying distance of MIMO array to the target. The amplitude factor (i.e., path loss) is typically ignored in the existing derivations. The target points are located at an average distance of z_0 from the aperture plane. Therefore, R^{-2} in (17) can be approximated by $(z_0 R)^{-1}$. The error introduced by this approximation will be negligible in the near-field applications [34]. z_0 is constant for a stationary object and, therefore, it can be ignored. As a result, the 2-D image reconstruction will be effectively approximated by a combination of the phase terms and the retained R^{-1} dependence that yields

$$s(x, y, k) = \iint p(x', y') \frac{e^{j2kR}}{R}\, dx'\, dy'. \tag{18}$$

Our derivation builds on the spirit of Weyl's idea [35] of the representation of a spherical wave as a superposition of plane waves [36]

$$\frac{e^{j2kR}}{R} = \frac{j}{2\pi} \iint \frac{e^{j(k_x(x-x')+k_y(y-y')+k_z z_0)}}{k_z}\, dk_x\, dk_y, \tag{19}$$

where

$$k_z = \sqrt{4k^2 - k_x^2 - k_y^2}. \tag{20}$$

It is important to note that the plane waves are homogeneous when $k_x^2 + k_y^2 \leq 4k^2$, but they are inhomogeneous (significant only close to the plane $z_0 = 0$) otherwise. The entire derivation of (19) is given in the Appendix B.

After substituting (19) into (18), the backscattered data becomes

$$s(x, y, k) = \frac{j}{2\pi} \iiint\!\!\iint p(x', y') \times \frac{1}{k_z} e^{j(k_x(x-x')+k_y(y-y')+k_z z_0)}\, dk_x\, dk_y\, dx'\, dy'. \tag{21}$$

Rearranging the order of integrals and using the 2-D Fourier transform definitions in the Appendix A gives

$$s(x, y, k) = \frac{j}{2\pi} \iint \underbrace{\left[\iint p(x', y') e^{-j(k_x x' + k_y y')}\, dx'\, dy' \right]}_{\mathrm{FT}_{2D}\left[p(x,y)\right] = P(k_x, k_y)} \times \frac{e^{jk_z z_0}}{k_z} e^{j(k_x x + k_y y)}\, dk_x\, dk_y. \tag{22}$$

The distinction between the primed and unprimed coordinate systems above is dropped in the forward Fourier transform operation (denoted as FT_{2D}) because they coincide. The outer double integral above represents a 2-D inverse Fourier transform over the xy domain. Hence, after dropping the constant terms, (22) becomes

$$s(x, y, k) = \mathrm{IFT}_{2D}\left[P(k_x, k_y) \frac{e^{jk_z z_0}}{k_z} \right], \tag{23}$$

that yields

$$P(k_x, k_y) = S(k_x, k_y, k) k_z e^{-jk_z z_0}. \tag{24}$$

In (23), IFT_{2D} denotes 2-D inverse Fourier transform operation over the xy domain. (24) is then evaluated at multiple wavenumbers and coherently summed within an image plane [16] to reconstruct the 2-D target reflectivity as

$$p(x, y) = \int \mathrm{IFT}_{2D}\left[S(k_x, k_y, k) k_z e^{-jk_z z_0} \right] dk. \tag{25}$$

Therefore, a monochromatic approach is assumed in the rest of the paper and k variable in the backscattered data is dropped for simplicity.

IV. DEVELOPMENT OF IMAGE RECONSTRUCTION WITH SPARSE MIMO-SAR

The mmWave imager proposed and prototyped in this paper exploits sparse MIMO array configurations to reduce the cost and scanning time while providing high-resolution imaging. To recover images without any reconstruction artifacts, we investigate the response of the sparsely sampled MIMO-SAR imaging system to the target being imaged by establishing properties between spectral and spatial domains. As a first step, we review the analysis of the 1-D $k-$domain spectrum in terms of the dimensions of the target and the continuous finite SAR aperture. This analysis will enable us to develop a novel Fourier based imaging formulation compatible with sparsely sampled MIMO-SAR data.

A. WAVENUMBER SPECTRUM ANALYSIS AND SAMPLING CRITERION

Consider an imaging scenario, where the target area is centered with respect to the scanning system, as depicted in Fig. 3. While the analysis of the wavenumber spectrum here is limited to $x-$axis, the expressions can be easily expanded to $y-$axis. This approach is based on a prior knowledge of the total size of the target region under consideration instead of an unknown physical target geometry.

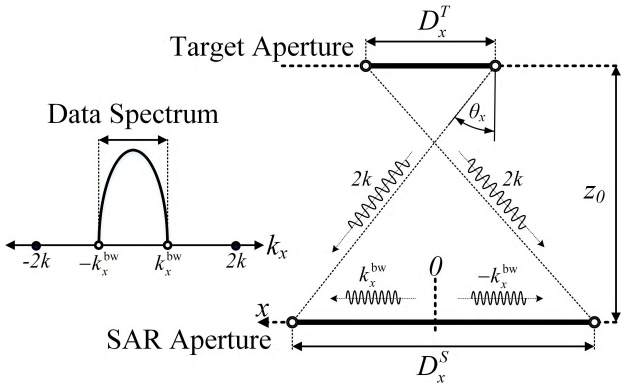

FIGURE 3. Spectral domain of the backscattered data in $x-$axis.

Denote θ_x as the limit of the system operating angle in $x-$axis, which is the lesser of the full beamwidth of the antenna or the angle covered by the aperture over the corresponding axis. Assuming the angle subtended by the aperture is less than the beamwidth of the antenna, we can express

$$\sin\theta_x = \frac{(D_x^S + D_x^T)/2}{\sqrt{(D_x^S + D_x^T)^2/4 + z_0^2}}, \tag{26}$$

where D_x^S and D_x^T are the SAR and target aperture sizes, respectively, as depicted in Fig. 1. As a result, the spectrum of the backscattered signal along $x-$axis will be limited to the region $[-k_x^{\text{bw}}, k_x^{\text{bw}}]$ where k_x^{bw} is the highest wavenumber component defined as

$$k_x^{\text{bw}} \approx 2k\sin\theta_x. \tag{27}$$

Substituting (26) into (27) yields the bandwidth of the backscattered data collected along $x-$axis as

$$k_x^{\text{bw}} \approx \frac{2\pi(D_x^S + D_x^T)}{\lambda\sqrt{(D_x^S + D_x^T)^2/4 + z_0^2}}. \tag{28}$$

In MIMO-SAR imaging configuration, the backscattered signals are spatially sampled by transmit/receive antenna locations. While the proposed system employs sparse sampling, its development will be facilitated by understanding of the spatial sampling requirements based on monostatic scenario. As in the traditional time domain signals, sampling needs to satisfy the Nyquist criterion to avoid aliasing, but in space. The maximum theoretical limit of monostatic sampling of infinite aperture is $\lambda/4$ where λ is the wavelength [4]. However, the spectrum of the backscattered data captured over a finite SAR aperture is limited by its size, spatial extent of the target aperture, and the distance between both apertures.

Consider a continuous spatial domain signal $s(x)$ captured in an imaging scheme in Fig. 3 and its Fourier transform (i.e., its wavenumber spectrum) $S(k_x)$. As expressed in (28), $S(k_x)$ is band-limited to $|k_x| \le k_x^{\text{bw}}$. The corresponding minimum sampling wavenumber (i.e., the Nyquist rate) along $x-$axis is given by

$$k_x^s \ge 2k_x^{\text{bw}} = \frac{4\pi(D_x^S + D_x^T)}{\lambda\sqrt{(D_x^S + D_x^T)^2/4 + z_0^2}}. \tag{29}$$

Hence, $s(x)$ can be perfectly reconstructed from its samples without aliasing as long as the spatial sampling interval is [5]

$$\Delta_x \le \Delta_x^{\text{Nyq}} = \frac{\pi}{k_x^{\text{bw}}} = \frac{\lambda\sqrt{(D_x^S + D_x^T)^2/4 + z_0^2}}{2(D_x^S + D_x^T)}. \tag{30}$$

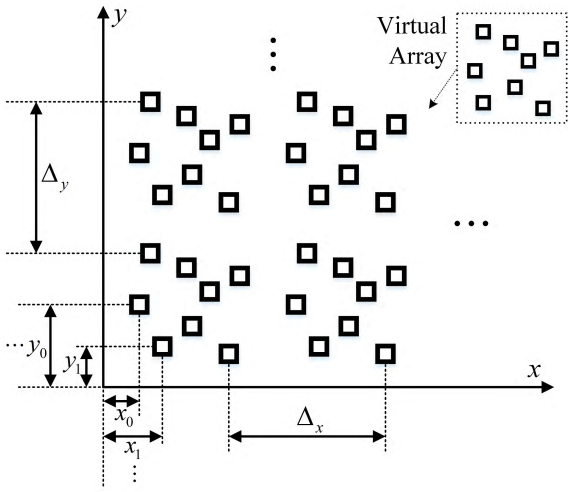

FIGURE 4. Illustration of periodically nonuniform sampling of the continuous two-dimensional SAR aperture.

B. ANALYSIS OF SPARSELY SAMPLED CONTINUOUS SAR APERTURE DATA

MIMO array configurations can be used to reduce the hardware cost, software complexity, and data acquisition time. Our imaging setup is based on a sparse MIMO array, which is scanned mechanically in a plane as shown in Fig. 1. The radar waveforms transmitted by the MIMO array sample the continuous xy plane as illustrated in Fig. 4. Based on the conversion of the MIMO array to the monostatic operation in (4) and the phase correction factor in (15), we can express spatially sampled version of the continuous SAR aperture data by the ℓth virtual channel as

$$s_\ell(x,y) = s(x,y)e^{j\phi_\ell} \times \sum_{p\in\mathbb{Z}}\sum_{q\in\mathbb{Z}} \delta(x - p\Delta_x - x_\ell, y - q\Delta_y - y_\ell), \tag{31}$$

where Δ_x and Δ_y are the sampling distances along x and y dimensions, respectively, as shown in Fig. 1. $s(x,y)$ above represents the backscattered data that would be received by a physical monostatic element over the continuous xy aperture. x_ℓ and y_ℓ are the virtual element midpoint offsets in x and y axes, respectively, as depicted in Fig. 4.

Using the Fourier transform definitions in Appendix A, we can express the 2-D wavenumber spectrum of the sampled signal associated with the ℓth channel as

$$S_\ell(k_x,k_y)=\frac{e^{j\phi_\ell}}{\Delta_x\Delta_y}\times\sum_{m\in\mathbb{Z}}\sum_{n\in\mathbb{Z}}S(k_x-mk_x^s,k_y-nk_y^s)\times e^{-j(mk_x^s x_\ell+nk_y^s y_\ell)},\tag{32}$$

subject to

$$(k_x-mk_x^s)^2+(k_y-nk_y^s)^2\le 4k^2,\quad \forall m,n\in\mathbb{Z},\tag{33}$$

where

$$k_x^s=\frac{2\pi}{\Delta_x},\quad k_y^s=\frac{2\pi}{\Delta_y},\tag{34}$$

are the spatial sampling frequencies.

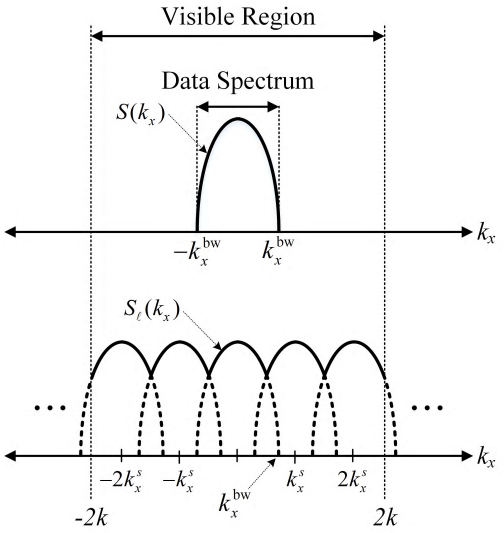

FIGURE 5. Wavenumber domain spectrum of the continuous SAR data and its sampled version along $x-$axis.

The imaging system working at a specific frequency range can be used to image targets with unknown sizes and proximity. Thus, our goal in this paper is to obtain the alias-free wavenumber spectrum within the visible region, $[-2k,2k]$. Due to sparsity of MIMO array and subsampling of the scene, the visible region can contain multiple aliasing components as shown in Fig. 5. The overlapping spectral components due to aliasing are centered at (mk_x^s,nk_y^s) for $\forall m,n\in\mathbb{Z}$ with $\{m,n\}\neq\{0,0\}$. We will focus on the visible region defined in (33) that limits the number of shifted copies as

$$|mk_x^s-k_x^{bw}|\le 2k,\quad |nk_y^s-k_y^{bw}|\le 2k.\tag{35}$$

Recall that the Nyquist rate of $k_x^s>4k$ (equivalently, $\Delta_x<\lambda/4$) ensures alias-free images within the visible region. However, our goal is to work with a sampling rate $k_x^s\ll 4k$.

C. EFFECT OF ALIASING ON THE IMAGE DOMAIN

Fourier transform properties are powerful tools for analyzing linear time invariant (LTI) systems. On the other hand, the relation between the wavenumber spectrum of the subsampled backscattered data and the reconstructed image is inherently nonlinear. To our knowledge, there is no prior work on establishing this nonlinear relation. Here, starting with the analysis in Section IV-B, we derive the analytical response of the reconstructed image to the aliasing components in the subsampled data spectrum.

Recall that the aliasing spectral component with index m and n (for $\{m,n\}\neq\{0,0\}$) of the ℓth subchannel is defined in (32) as

$$S_{mn}^\ell(k_x,k_y)=\underbrace{\frac{e^{j(\phi_\ell-(mk_x^s x_\ell+nk_y^s y_\ell))}}{\Delta_x\Delta_y}}_{C_{mn}^\ell}S(\hat{k}_x,\hat{k}_y),\tag{36}$$

where

$$\hat{k}_x=k_x-mk_x^s,\quad \hat{k}_y=k_y-nk_y^s.\tag{37}$$

Using the relation between the backscattered data and the image spectra in (24), (36) becomes

$$S_{mn}^\ell(k_x,k_y)=C_{mn}^\ell P(\hat{k}_x,\hat{k}_y)\frac{e^{j\hat{k}_z z_0}}{\hat{k}_z},\tag{38}$$

where

$$\hat{k}_z=\sqrt{4k^2-(\hat{k}_x)^2-(\hat{k}_y)^2}.\tag{39}$$

Substituting (38) into (24) yields the wavenumber spectrum of the imaging artifact (i.e., ghost image) created by the aliasing component as

$$\begin{aligned}P_{mn}^\ell(k_x,k_y)&=S_{mn}^\ell(k_x,k_y)k_z e^{-jk_z z_0}\\&=C_{mn}^\ell P(\hat{k}_x,\hat{k}_y)\frac{k_z}{\hat{k}_z}e^{j(\hat{k}_z-k_z)z_0}.\end{aligned}\tag{40}$$

From (20) and (39), let us define the amplitude and the phase terms in (40) as

$$\vartheta(k_x,k_y)=\frac{k_z}{\hat{k}_z}=\frac{\sqrt{4k^2-k_x^2-k_y^2}}{\sqrt{4k^2-\hat{k}_x^2-\hat{k}_y^2}},\tag{41}$$

and

$$\begin{aligned}\varphi(k_x,k_y)&=(\hat{k}_z-k_z)z_0\\&=\left(\sqrt{4k^2-\hat{k}_x^2-\hat{k}_y^2}-\sqrt{4k^2-k_x^2-k_y^2}\right)z_0.\end{aligned}\tag{42}$$

Applying first-order multivariate Taylor series expansion to (41) and (42) with respect to the parameters (k_x,k_y) around (mk_x^s,nk_y^s), as described in the Appendix C, the linear approximations of the amplitude and the phase terms become

$$\vartheta(k_x,k_y)\approx\underbrace{\frac{2k}{G_{mn}}}_{\vartheta_{mn}}-\underbrace{\frac{mk_x^s}{2kG_{mn}}}_{\hat{x}_{mn}}k_x-\underbrace{\frac{nk_y^s}{2kG_{mn}}}_{\hat{y}_{mn}}k_y,$$

$$\varphi(k_x,k_y)\approx \underbrace{2kz_0\left(1-\frac{2k}{G_{mn}}\right)}_{\varphi_{mn}}+\underbrace{\frac{mk_x^s z_0}{G_{mn}}}_{x_{mn}}k_x+\underbrace{\frac{nk_y^s z_0}{G_{mn}}}_{y_{mn}}k_y, \quad (43)$$

where

$$G_{mn}=\sqrt{4k^2-(mk_x^s)^2-(nk_y^s)^2}. \quad (44)$$

Substituting (43) into (40), the wavenumber spectrum of the ghost image is approximated as

$$P_{mn}^{\ell}(k_x,k_y)\approx C_{mn}^{\ell}P(\hat{k}_x,\hat{k}_y)e^{j\varphi_{mn}}\times(\vartheta_{mn}-\hat{x}_{mn}k_x-\hat{y}_{mn}k_y)\times e^{j(k_x x_{mn}+k_y y_{mn})}. \quad (45)$$

Using (37) and (45), let us define

$$Q_{mn}^{\ell}(k_x,k_y)=(\alpha_{mn}^{\ell}-\beta_{mn}^{\ell}k_x-\gamma_{mn}^{\ell}k_y)\times P(k_x-mk_x^s,k_y-nk_y^s), \quad (46)$$

where

$$\begin{aligned}\alpha_{mn}^{\ell}&=\vartheta_{mn}C_{mn}^{\ell}e^{j\varphi_{mn}}\\ \beta_{mn}^{\ell}&=\hat{x}_{mn}C_{mn}^{\ell}e^{j\varphi_{mn}}\\ \gamma_{mn}^{\ell}&=\hat{y}_{mn}C_{mn}^{\ell}e^{j\varphi_{mn}}.\end{aligned} \quad (47)$$

Substituting (46) into (45) yields

$$P_{mn}^{\ell}(k_x,k_y)\approx Q_{mn}^{\ell}(k_x,k_y)e^{j(k_x x_{mn}+k_y y_{mn})}. \quad (48)$$

Using the Fourier transform definitions in the Appendix A, the ghost image created by the aliasing component is calculated as

$$p_{mn}^{\ell}(x,y)\approx q_{mn}^{\ell}(x+x_{mn},y+y_{mn}), \quad (49)$$

where (from (46))

$$\begin{aligned}q_{mn}^{\ell}(x,y)&=\mathrm{IFT}_{2D}\left[Q_{mn}^{\ell}(k_x,k_y)\right]\\&=\alpha_{mn}^{\ell}e^{j(mk_x^s x+nk_y^s y)}p(x,y)\\&\quad+j\beta_{mn}^{\ell}e^{jnk_y^s y}\frac{\partial(e^{jmk_x^s x}p(x,y))}{\partial x}\\&\quad+j\gamma_{mn}^{\ell}e^{jmk_x^s x}\frac{\partial(e^{jnk_y^s y}p(x,y))}{\partial y}.\end{aligned} \quad (50)$$

Hence, from (49) and (50), the ghost image created by an aliasing component in the subsampled wavenumber spectrum is the nonlinear operated alias-free image shifted by

$$x_{mn}=\frac{mk_x^s z_0}{G_{mn}},\quad y_{mn}=\frac{nk_y^s z_0}{G_{mn}}. \quad (51)$$

D. IMAGE RECONSTRUCTION WITH SPARSELY SAMPLED MIMO-SAR DATA

As given in Section IV-B, if the spatial sampling intervals Δ_x and Δ_y do not meet the Nyquist criterion, aliasing that creates artifacts (i.e., ghosts) in the reconstructed image will occur as detailed in Section IV-C. Here, we propose a method for a sparse MIMO-SAR configuration to perfectly reconstruct alias-free images based on a multichannel combining technique using properly chosen complex gains. In other words, we show that the aliasing components in (36), which creates ghost images in (49), can be canceled by properly choosing a complex gain vector

$$\mathbf{w}=\begin{bmatrix}w_0 & w_1 & \dots & w_{L-1}\end{bmatrix}^T, \quad (52)$$

for L virtual channels, where $(.)^T$ denotes the transpose operation. The flow diagram of the MIMO-SAR sampling (as given in (31)) and the proposed image reconstruction scheme is depicted in Fig. 6.

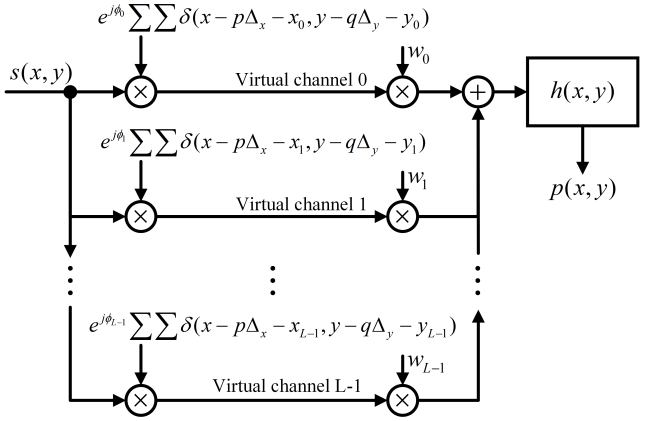

FIGURE 6. Reconstruction of image using sparsely sampled backscattered data by L virtual channels.

Recall that the image reconstruction filter $h(x,y)$ in Fig. 6 is given in (24) as

$$h(x,y)=\mathrm{IFT}_{2D}\left[k_z e^{-jk_z z_0}\right], \quad (53)$$

where k_z is given in (20) and IFT_{2D} denotes 2-D inverse Fourier transform operation over the xy domain. Combination of L subchannel spectrum in (32) using the complex gain vector in (52) is expressed as

$$\tilde{S}(k_x,k_y)=\sum_{\ell=0}^{L-1}w_\ell S_\ell(k_x,k_y)=\frac{1}{\Delta_x\Delta_y}\sum_{\ell=0}^{L-1}w_\ell e^{j\phi_\ell}\times\sum_{<m>}\sum_{<n>}S(k_x-mk_x^s,k_y-nk_y^s)e^{-j(mk_x^s x_\ell+nk_y^s y_\ell)}. \quad (54)$$

In Section IV-B, we analyze the number of shifted copies in the wavenumber spectrum that must be canceled to reconstruct alias-free images of the targets with unknown sizes and proximity. Therefore, (35) yields the total number copies within the entire visible region. However, for a finite SAR aperture configuration with a prior knowledge of the target (see Section IV-A), the total number of aliasing terms in (54) that has to be canceled is limited by the indexes m and n as

$$|mk_x^s|\le 2k_x^{\mathrm{bw}},\quad |nk_y^s|\le 2k_y^{\mathrm{bw}}, \quad (55)$$

where k_x^{bw} and k_y^{bw} are the highest wavenumber components in x and y axes, respectively, as detailed in Section IV-A. Using the following vector notation

$$\boldsymbol{\alpha}_{m,n}=\begin{bmatrix}mk_x^s & nk_y^s\end{bmatrix},\quad \boldsymbol{\beta}_\ell=\begin{bmatrix}x_\ell & y_\ell\end{bmatrix}^T, \quad (56)$$

we can rearrange (54) as

$$\begin{aligned}\tilde{S}(k_x,k_y) = \frac{1}{\Delta_x\Delta_y}\Bigg[&\left(\sum_{\ell=0}^{L-1} w_\ell e^{j\phi_\ell}\right)S(k_x,k_y)\\ &+\left(\sum_{\ell=0}^{L-1} w_\ell e^{j(\phi_\ell-\boldsymbol{\alpha}_{0,1}\boldsymbol{\beta}_\ell)}\right)S(k_x,k_y-k_y^s)\\ &+\left(\sum_{\ell=0}^{L-1} w_\ell e^{j(\phi_\ell-\boldsymbol{\alpha}_{0,2}\boldsymbol{\beta}_\ell)}\right)S(k_x,k_y-2k_y^s)+\ldots\\ &+\left(\sum_{\ell=0}^{L-1} w_\ell e^{j(\phi_\ell-\boldsymbol{\alpha}_{1,0}\boldsymbol{\beta}_\ell)}\right)S(k_x-k_x^s,k_y)+\ldots\Bigg].\end{aligned} \tag{57}$$

Therefore, if the equation below has a solution for $\mathbf{w}$, all the aliasing terms are canceled to obtain alias-free backscattered data wavenumber spectrum $S(k_x, k_y)$ in (57)

$$\underbrace{\begin{bmatrix} e^{j\phi_0} & e^{j\phi_1} & \ldots & e^{j\phi_{L-1}}\\ e^{j(\phi_0-\boldsymbol{\alpha}_{0,1}\boldsymbol{\beta}_0)} & e^{j(\phi_1-\boldsymbol{\alpha}_{0,1}\boldsymbol{\beta}_1)} & \ldots & e^{j(\phi_{L-1}-\boldsymbol{\alpha}_{0,1}\boldsymbol{\beta}_{L-1})}\\ e^{j(\phi_0-\boldsymbol{\alpha}_{0,2}\boldsymbol{\beta}_0)} & e^{j(\phi_1-\boldsymbol{\alpha}_{0,2}\boldsymbol{\beta}_1)} & \ldots & e^{j(\phi_{L-1}-\boldsymbol{\alpha}_{0,2}\boldsymbol{\beta}_{L-1})}\\ \vdots & \vdots & \vdots & \vdots\\ e^{j(\phi_0-\boldsymbol{\alpha}_{1,0}\boldsymbol{\beta}_0)} & e^{j(\phi_1-\boldsymbol{\alpha}_{1,0}\boldsymbol{\beta}_1)} & \ldots & e^{j(\phi_{L-1}-\boldsymbol{\alpha}_{1,0}\boldsymbol{\beta}_{L-1})}\\ \vdots & \vdots & \vdots & \vdots \end{bmatrix}}_{\mathbf{A}} \times \underbrace{\begin{bmatrix} w_0\\ w_1\\ \vdots\\ w_{L-1}\end{bmatrix}}_{\mathbf{w}} = \Delta_x\Delta_y \underbrace{\begin{bmatrix}1\\0\\ \vdots\\0\end{bmatrix}}_{\mathbf{e}}. \tag{58}$$

Hence, expanding the reconstruction formula in (25), the solution for the gain vector in (58)

$$\mathbf{w} = (\mathbf{A}^H\mathbf{A})^{-1}\mathbf{A}^H\mathbf{e}, \tag{59}$$

finally yields the 2-D monochromatic image reconstruction for MIMO-SAR as

$$p(x,y) = \mathrm{IFT}_{2D}\left[\mathbf{w}^T\mathbf{S}(k_x,k_y)k_z e^{-jk_z z_0}\right], \tag{60}$$

where

$$\mathbf{S}(k_x,k_y) = \begin{bmatrix}S_0(k_x,k_y) & \ldots & S_{L-1}(k_x,k_y)\end{bmatrix}^T, \tag{61}$$

is constructed by the wavenumber spectrum of the backscattered data sampled by L virtual channels. In (59), $(.)^{-1}$ denotes the inverse and $(.)^H$ denotes the conjugate transpose of a matrix. Using the same approach in (25), (60) is then evaluated at multiple wavenumbers and coherently summed within the image plane. As detailed in Section IV-B, each subchannel data $s_\ell(x, y)$ is uniformly sampled over the xy domain. Therefore, the 2-D fast Fourier transform (FFT) may be used to obtain a sampled version of $S_\ell(k_x, k_y)$. Assuming a discretization of $N_x \times N_y$ points in the continuous xy plane with N_k sample points in the wavenumber domain, the computational complexity of the image reconstruction, which is dominated by the 2-D FFT operations in (61), can be approximated as $LN_xN_yN_k(\log(N_x) + \log(N_y))$.

It is important to note that, using the complex gains in (59), $L-1$ aliasing terms can be canceled using L subchannels. The proposed imaging method makes no assumption on the positions of the transmitters and receivers as long as the antenna layout and the sampling scenario ensure a well-conditioned $\mathbf{A}$ matrix in (58). Therefore, the proposed algorithm can be used for MIMO-SAR configurations using arbitrarily distributed transmit and receive antennas.

V. IMAGE RESOLUTION

The theoretical limit of the spatial resolution achieved in the reconstructed image is determined by width of the coverage in the wavenumber spectrum domain. In one dimension, a spectral coverage of width Δk results in a spatial pulsewidth of $2\pi/\Delta k$ [4]. The spatial frequency width of the backscattered data in k_z-axis is $2(k_T - k_0)$, where k_0 and k_T are the wavenumbers correspond to the lowest and highest operating frequencies of the system (f_0 and f_T, respectively, in (14)). Therefore, the depth ($z-$axis) resolution is determined by the bandwidth as

$$\delta_z \approx \frac{2\pi}{2(k_T-k_0)} = \frac{c}{2(f_T-f_0)} = \frac{c}{2B}. \tag{62}$$

Similarly, from Section IV-A, the total bandwidth in the x and y axes are

$$\begin{aligned}\Delta k_x &\approx 2k_x^{\mathrm{bw}} \approx \frac{4\pi(D_x^S+D_x^T)}{\lambda\sqrt{(D_x^S+D_x^T)^2/4+z_0^2}},\\ \Delta k_y &\approx 2k_y^{\mathrm{bw}} \approx \frac{4\pi(D_y^S+D_y^T)}{\lambda\sqrt{(D_y^S+D_y^T)^2/4+z_0^2}},\end{aligned} \tag{63}$$

where the physical lengths of the SAR aperture and the target distance are depicted in Fig. 1. Hence, the horizontal ($x-$axis) and vertical ($y-$axis) cross-range resolutions become

$$\begin{aligned}\delta_x &\approx \frac{2\pi}{\Delta k_x} \approx \frac{\lambda\sqrt{(D_x^S+D_x^T)^2/4+z_0^2}}{2(D_x^S+D_x^T)},\\ \delta_y &\approx \frac{2\pi}{\Delta k_y} \approx \frac{\lambda\sqrt{(D_y^S+D_y^T)^2/4+z_0^2}}{2(D_y^S+D_y^T)}.\end{aligned} \tag{64}$$

For an aperture-limited system with range z_0 much greater than the aperture size D_x^S and D_y^S, the cross-range resolutions can be approximated for the center of the imaging scene (i.e. $D_x^T = D_y^T = 0$) as [4], [5]

$$\delta_x \approx \frac{\lambda z_0}{2D_x^S}, \quad \delta_y \approx \frac{\lambda z_0}{2D_y^S}. \tag{65}$$

VI. IMAGING HARDWARE PROTOTYPE

A. SYSTEM OVERVIEW

A mmWave imaging prototype system has been built using commercial off-the-shelf (COTS) components to validate

the proposed image reconstruction techniques and theoretical relationships established between image and wavenumber domains. The prototype system consists of a mmWave radar, a two-axis mechanical scanner, a motor controller, and a host personal computer (PC). The mmWave radar is combination of three hardware modules from Texas Instruments: (1) IWR1443-Boost, (2) mmWave-Devpack, and (3) TSW1400 boards as shown in Fig. 7a.

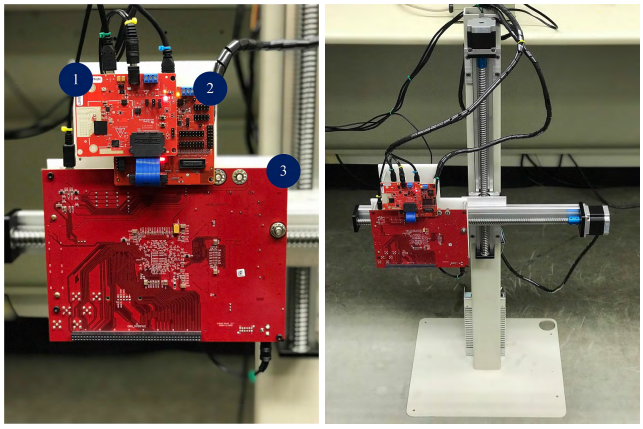

FIGURE 7. mmWave imager prototype. (a) FMCW radar hardware stack. (b) Two-axis motorized scanner.

IWR1443-Boost is an evaluation module based on the single-chip IWR1443 mmWave sensor. It features FMCW transceiver with a 4 GHz frequency bandwidth from 77 GHz to 81 GHz. It integrates four receive and three transmit antennas making an ideal candidate for sparse MIMO array configurations. Fig 8a shows the physical antenna layout of IWR1443-Boost and its corresponding virtual array configuration. In the default layout, the receive antennas are uniformly spaced along $y-$axis by $\lambda/2$ (tuned to the center frequency of 79 GHz). Transmit antennas are also uniformly spaced in $y-$axis by λ with the exception of the second transmitter, which has an offset of $\lambda/2$ along $x-$axis. In the imaging experiments, we select different antenna pairs (i.e., virtual channels) to emulate various sparse MIMO operations.

TSW1400 and mmWave-Devpack are add-on boards used with IWR1443-Boost to enable high speed raw data capture for post processing. Captured raw data are imported to the host PC with a serial port for the image reconstruction. All algorithms and software controls are implemented in MATLAB.

The other component of the prototype system is the two-axis mechanical scanner built using linear rails and stepper motors, as shown in Fig. 7b. The scanner provides movements in horizontal and vertical directions. The radar hardware stack is installed on the horizontal track by which an equivalent 2-D scanning is achieved. The maximum scanning ranges in both horizontal and vertical directions are 400 mm. The motor controller, which is configured to operate linear rails at a maximum speed of 20 mm/s, is connected to the host PC with a serial port. The positional accuracy of the scanning is about 0.05 mm. While the current scanner is slow, our goal is to demonstrate the proof of concept. We are working on a much faster mechanical scanner, and we will report our results in a future article.

The diagram shown in Fig. 8b is a simplified view of the main elements and the high-level system architecture of the imaging system. Both radar and rail system are controlled via a MATLAB graphical user interface (GUI) shown in Fig. 9.

B. MIMO ARRAY CALIBRATION

In a practical system, measurement errors in the MIMO array may arise due to sensor gain and phase mismatches. Especially, phase mismatches can affect the image reconstruction adversely. In fact, the algorithms proposed in this paper are derived under the assumption that the response of the imaging system is known.

In this paper, we utilize a well-known calibration method for multistatic radar systems based on the ideal backscattered signal model from a reference point target (a corner reflector) at a known position. Let us define the total round-trip delay $\tilde{\tau}_\ell$ of the FMCW signal reflected off the point target between the uth transmit and vth receive antennas, and the corresponding transceiver gain a_ℓ. We model the delays between antenna pairs as the superposition of a common instrument delay and residual delays between antenna elements: $\tilde{\tau}_\ell = \tau_i + \tau_\ell$. Ignoring the additive noise, the uncalibrated measured beat signal (see Section II-D) can be defined as

$$\tilde{s}_\ell(t) = a_\ell e^{j2\pi(f_0+Kt)(\tau_i+\tau_\ell)} = \underbrace{\underbrace{a_\ell e^{j\psi_i}}_{\eta_\ell} e^{j2\pi f_i t}}_{w_\ell(t)} s_\ell(t), \quad (66)$$

where $s_\ell(t)$ is the reference beat signal model, $f_i = K\tau_i$ is the beat frequency that cause a range bias in the system, and η_ℓ is the residual complex gain factor. Given the measurements $\tilde{s}_\ell(t)$, the calibration error signal can be computed by a simple demodulation process

$$w_\ell(t) = \tilde{s}_\ell(t) s_\ell^*(t), \quad (67)$$

where $(.)^*$ denotes the complex-conjugate operation. Estimating f_i and η_ℓ from (67) reduces to the parameter estimation problem of a single-frequency complex tone from noisy observations [37], [38]

$$\hat{f}_i = \arg\max_f \sum_{<\ell>} |W_\ell(f)|^2, \quad (68)$$

where $W_\ell(f)$ is defined as

$$W_\ell(f) = \int_0^T w_\ell(t) e^{-j2\pi ft}\, dt. \quad (69)$$

Finally, the complex gain factors η_ℓ for each transceiver pair can be computed by plugging the estimate $\hat{f}_i$ in (66).

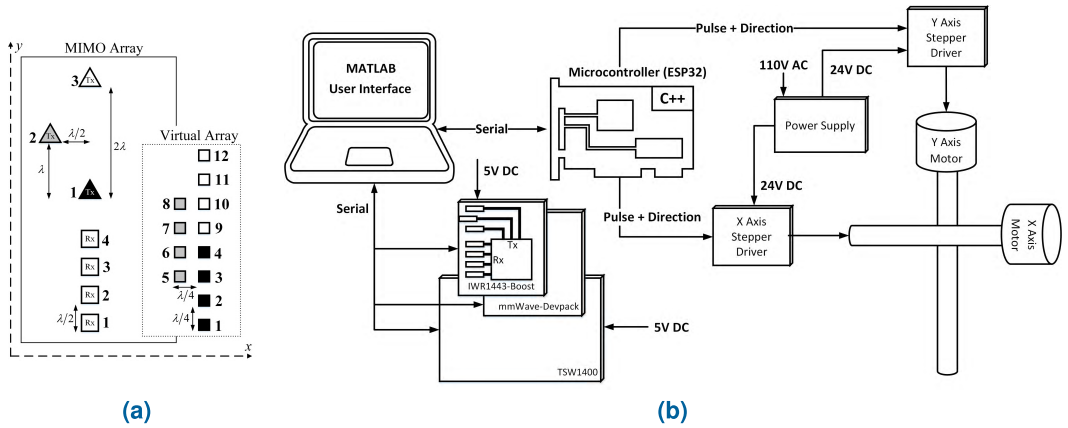

FIGURE 8. (a) MIMO array topology of IWR1443-Boost with three transmit and four receive antenna elements, and corresponding virtual array. (b) The hardware architecture of mmWave imager prototype.

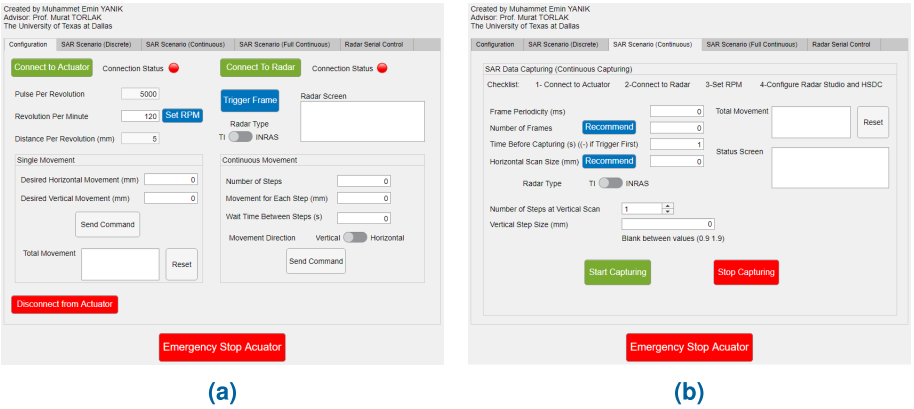

FIGURE 9. MATLAB GUI for MIMO-SAR imaging. (a) Platform and radar configuration menu tab. (b) SAR scenario generation menu tab.

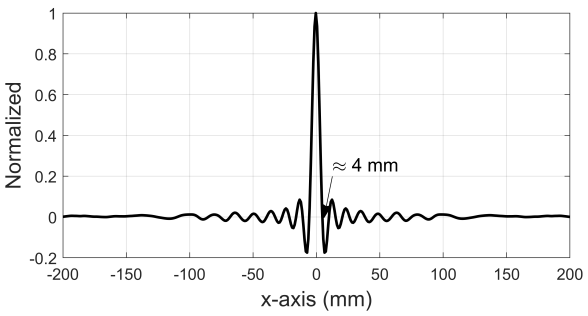

FIGURE 10. Measured PSF along $x-$axis provides the lateral image resolution that can be achieved by the imaging prototype system at a distance of 808 mm.

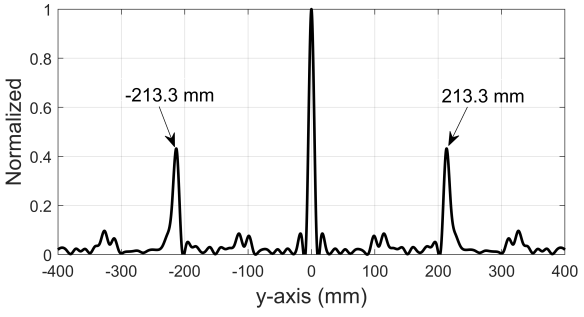

FIGURE 11. Measured PSF along $y-$axis demonstrates the impact of subsampling in spatial domain. Two visible artifacts are due to aliasing within the visible region.

VII. MEASUREMENTS AND IMAGING RESULTS

The reconstruction quality of the imaging systems is described by the point spread function (PSF). We measure the PSF of our system using a corner reflector. Then, simulations are performed to examine the potential of the proposed algorithms. Finally, the experimental image results of uncovered and concealed targets are provided. In all experiments, FMCW waveforms are configured to vary from $f_0 = 77.38$ GHz to $f_T = 80.93$ GHz, where the signal duration $T \approx 56.02\ \mu$s and the frequency slope $K \approx 63.37$ MHz/μs. The wavelength λ is computed according to the center frequency of 79 GHz unless otherwise noted. The target distance z_0 is estimated from the index of the maximum of the combined range spectrum computed

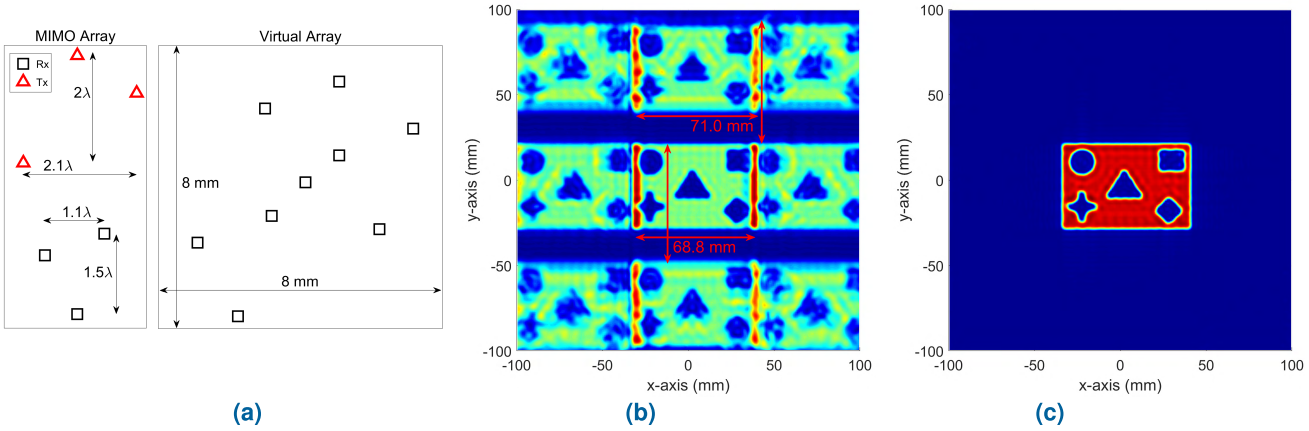

FIGURE 12. Simulated image reconstruction scenario with sparsely sampled aperture data: (a) simulated sparse MIMO array with three transmit and three receive antenna elements, and corresponding virtual array, (b) reconstructed image from single channel (1st), and (c) reconstructed image from nine channels combined using properly chosen *w* gains.

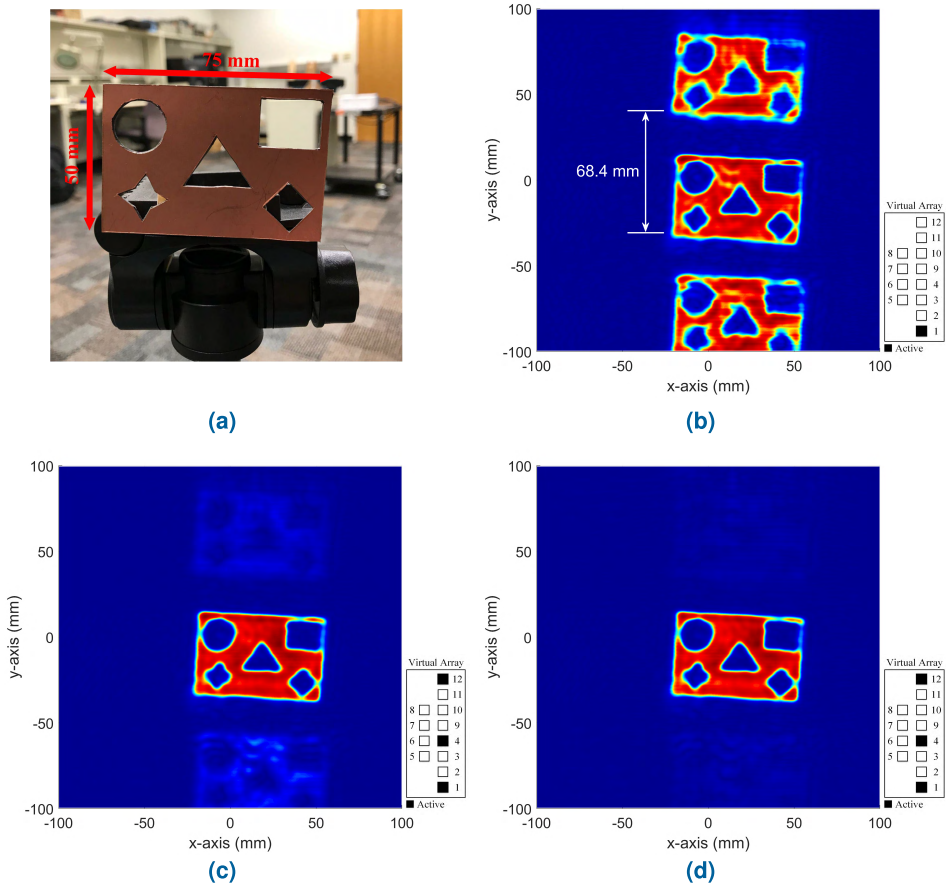

FIGURE 13. Various experimental images of the small test target: (a) optical, (b) reconstructed from single channel (1st), (c) reconstructed from three channels (1st, 4th, and 12th) combined without any correction factor, and (d) reconstructed from three channels (1st, 4th, and 12th) combined using properly chosen *w* gains.

from the beat signals. The image slices obtained at multiple frequencies from $f_0 = 77.38$ GHz to $f_T = 80.93$ GHz are coherently combined to form the final image. Before the image reconstruction process, each subchannel is calibrated as detailed in Section VI-B. All the images presented here are reconstructed on a host PC with Intel Core i7-7700 3.6 GHz central processing unit (CPU) and 64 gigabytes of random access memory (RAM).

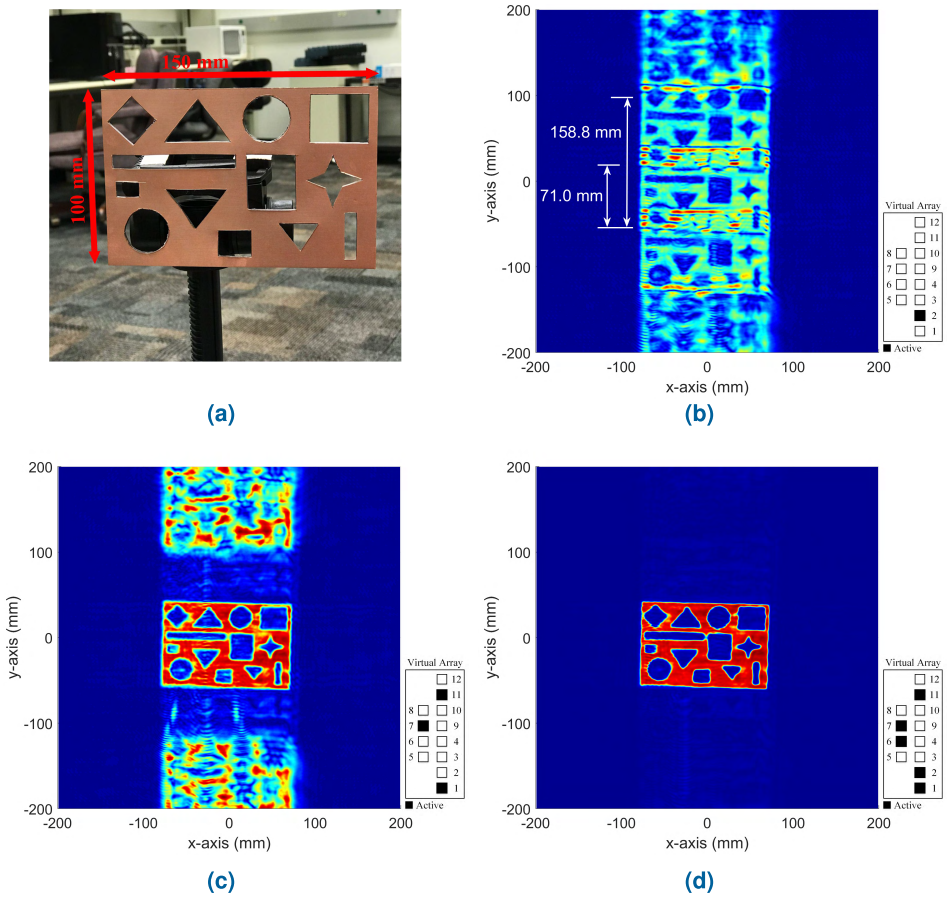

FIGURE 14. Various experimental images of the big test target: (a) optical, (b) reconstructed from single channel (2nd), (c) reconstructed from three channels (1st, 7th, and 11th) combined using properly chosen w gains, and (d) reconstructed from five channels (1st, 2nd, 6th, 7th, and 11th) combined using properly chosen w gains.

A. MEASURED POINT SPREAD FUNCTION

To demonstrate the experimental image resolution of our hardware prototype, we measure the PSF along $x-$axis between a transmit and receive antenna pair of MIMO radar. The measured PSF is shown in Fig. 10. In this measurement, a corner reflector is placed at a distance of $z_0 = 808$ mm in front of the scanner. The scanner moves the radar along $x-$axis. The speed of the scan and radar chirp intervals are configured such that a sampling distance of $\Delta_x \approx 0.96$ mm ($\approx \lambda/4$) is realized. The SAR aperture length is $D_x^S = 400$ mm along the scanning direction. As given in (64), the theoretical image resolution under this configuration is about $\delta_x \approx 4$ mm. As shown in Fig. 10, the measured PSF demonstrates the same theoretical image resolution.

An important contribution of this investigation is to establish the analytical relationship between imaging ambiguities and the subsampled SAR aperture parameters. The measured response of a single transceiver pair along $y-$axis generated with a sampling distance of $\Delta_y = 7.59$ mm (well over the required Nyquist interval) shows the presence of two imaging artifacts (i.e., ghosts), as shown in Fig. 11. In this experiment, the same corner reflector is placed at a distance of $z_0 = 808$ mm in front of the imager. The radar is configured with the same chirp parameters. We verify the positions of two artifacts along the $y-$axis due to subsampling using the expression in (51) as

$$y_{mn}|_{(m=0,n=\pm 1)} = \pm \frac{k_y^s z_0}{\sqrt{4k^2 - (k_y^s)^2}} \approx 213.3 \text{ mm},$$

at the center frequency of $f_0 = 77.38$ GHz, where the ghost image positions marked in Fig. 11 confirm the estimated ones above.

B. SIMULATED IMAGING RESULTS

To evaluate the performance of the proposed algorithm for recovering ghost-free images when both axes are subsampled, a simulation scenario is performed. A 50 mm by 75 mm small test target, which has different types of small cutouts, is simulated and placed at a distance of $z_0 = 282$ mm from the scanner. The size of the SAR aperture is $D_x^S \approx 200$ mm by $D_y^S \approx 200$ mm. The spatial sampling intervals are selected as $\Delta_x = \Delta_y = 8$ mm. An arbitrary sparse MIMO array with three transmit and three receive antennas shown in Fig.12a is simulated.

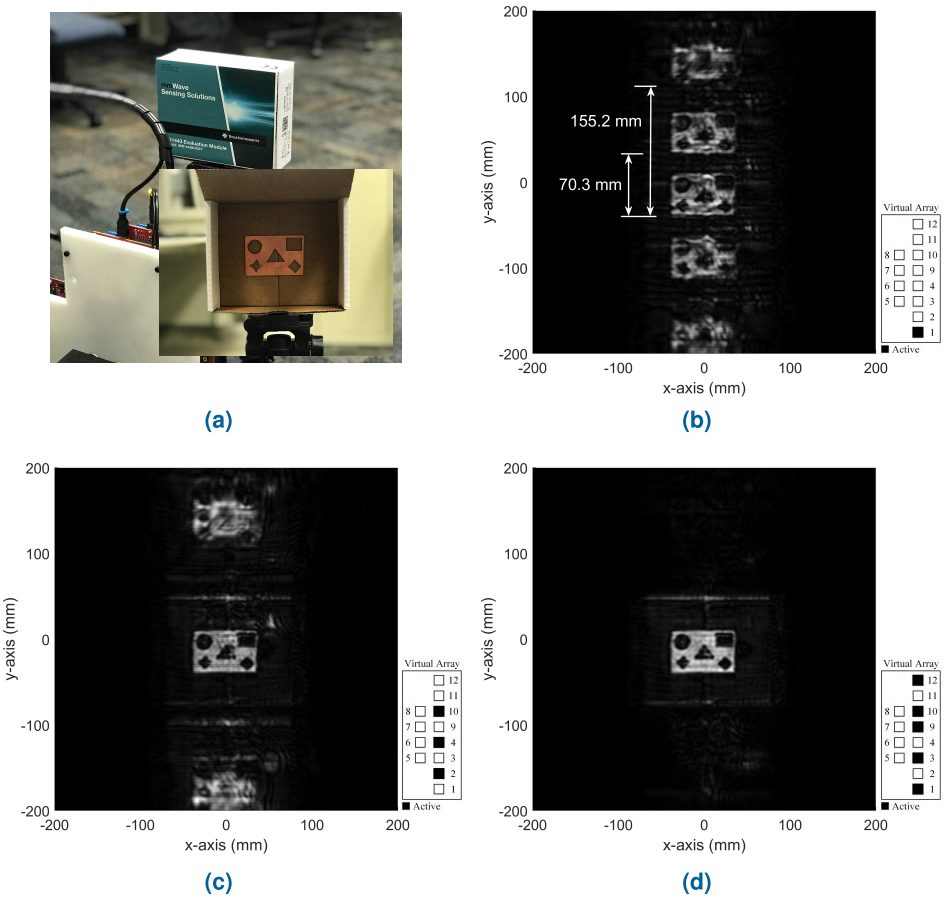

FIGURE 15. Various experimental images of the small test target concealed in a cardboard box: (a) optical, (b) reconstructed from single channel (1st), (c) reconstructed from three channels (2nd, 4th, and 10th) combined using properly chosen w gains, and (d) reconstructed from five channels (1st, 3rd, 9th, 10th, and 12th) combined using properly chosen w gains.

SAR aperture is subsampled along both x and y axes. The reconstructed image shown in Fig. 12b using a single virtual channel shows eight ghosts targets within the visible region of 200 mm $\times$ 200 mm as expected. The ghosts are located at a distance of (0, $\pm$68.8 mm), ($\pm$68.8 mm, 0), and ($\pm$71.0 mm, $\pm$71.0 mm) from the correct target as predicted in (51). Fig. 12c shows the alias-free image obtained using nine sparse channels with properly chosen w gains such that the all eight ghosts are canceled. On the other hand, an ideal imaging system, which needs $\lambda/4 \approx 0.95$ mm spacing between the measurement points, would employ a uniform 2-D array with about 80 virtual elements.

C. EXPERIMENTAL IMAGING RESULTS

The imaging process and the proposed image reconstruction algorithms with subsampled SAR aperture are experimentally verified with screening various targets. The antenna layout of IWR1443-Boost in Fig. 8a enables to emulate sparse MIMO configurations along $y-$axis. Therefore, in all experiments, we configure the MIMO-SAR setup in Fig. 1 to create various sparsely sampled aperture scenarios along $y-$axis. As discussed in Section II-B, TDM technique is employed across the transmitters of IWR1443-Boost module. Table 1 summarizes the common system parameters used in each experiment.

TABLE 1. Summary of the system parameters for each experiment.

Parameter	Fig. 13	Fig. 14	Fig. 15	Fig. 16	Fig. 17
B (GHz)	3.55	3.55	3.55	3.55	3.55
K (MHz/μs)	63.37	63.37	63.37	63.37	63.37
T (μs)	56.02	56.02	56.02	56.02	56.02
D_x (mm)	200	400	200	400	400
D_y (mm)	200	400	200	400	400
z_0 (mm)	280	275	288	270	254
Δ_x (mm)	0.98	0.98	0.98	0.98	0.98
Δ_y (mm)	8	7.59	8	7.59	7.59

A small test target with a size of 50 mm by 75 mm is cut out from a copper clad laminate to create a similar imaging setup to simulations. The test target has similar small cutouts as shown in Fig. 13a. In this scenario, the target is placed at a distance of $z_0 = 280$ mm from the scanner. The SAR aperture is synthesized to cover an area of $D_x^S \approx 200$ mm

by $D_y^S \approx 200$ mm. This configuration provides the lateral resolution of $\delta_x = \delta_y \approx 3$ mm. The spatial sampling intervals are selected as $\Delta_x \approx 0.98$ mm and $\Delta_y = 8$ mm along x and y axes, respectively. The measurement time required to scan the entire aperture, which is limited by the relatively slow linear rails as discussed in Section VI-A, is about 4 min.

The sampling interval along $x-$axis satisfies the Nyquist criterion. On the other hand, SAR aperture along $y-$axis is subsampled. The reconstructed image shown in Fig. 13b using a single virtual channel shows two obvious ghosts (false copies) along $y-$axis within the visible region of 200 mm $\times$ 200 mm. The correct target suffered from aliasing is at the center of the image. The ghosts are located at a distance of ± 68.4 mm (for $m = 0$ and $n = \pm 1$) from the correct target as predicted by theoretical results. Fig. 13c shows the image reconstructed by coherently combining the signals from the 1st, 4th, and 12th virtual channels without any correction factor. The ghosts due to aliasing are partially removed but not completely. In Fig. 13d, the reconstruction method presented in Section IV-D is applied and the spectrum from the same subchannels are coherently combined with the properly computed weights w from (59) to eliminate all ghosts. This demonstrates that the image can be reconstructed without aliasing in a subsampled scenario ($\Delta_y = 8$ mm $> 2\lambda$) using a sparse virtual array. The reconstruction of the image slices at each frequency takes less than 100 ms. Hence, the processing time of the final image formation using 64 uniformly spaced frequencies is about 6 s. The latency introduced by MATLAB would be considered in real-time practical implementations.

In the second imaging experiment, a bigger test target with dimensions 100 mm by 150 mm (shown in Fig. 14a) is cut to illustrate the distortion due to aliasing more effectively. The target distance is $z_0 = 275$ mm and the SAR aperture size is about 400 mm$\times$400 mm. Under this configuration, the lateral resolution is approximately 1.6 mm. The spatial sampling intervals are selected as $\Delta_x \approx 0.98$ mm and $\Delta_y = 7.59$ mm.

The sampling interval along $x-$axis satisfies the Nyquist criterion. However, the aperture is subsampled along $y-$axis. Fig. 14b shows the reconstructed image from a single channel. The image has four ghosts within a visible region of 400 mm $\times$ 400 mm. The ghosts are located at a distance of ± 71.0 mm and ± 158.8 mm (for $m = 0$, $n = \pm 1$, and $n = \pm 2$) from the correct target, as predicted by theoretical expressions. Fig. 14c shows the image obtained by combining signals from the 1st, 7th, and 11th channels with properly chosen w gains such that the first two ghosts are canceled. Fig. 14d shows the ghost-free image obtained using the 1st, 2nd, 6th, 7th, and 11th channels.

The third imaging experiment demonstrates the capability of the prototyped system for screening of concealed items. The smaller test target in Fig. 13a is concealed in a cardboard box as shown in Fig. 15a. The box is placed at a distance of $z_0 = 288$ mm from the scanner. The SAR aperture size and the spatial sampling intervals are same as the first imaging experiment. Therefore, the imaging scenario is subsampled along $y-$axis. The reconstructed image of a single channel shown in Fig. 15b shows four ghost targets within a visible region of 400 mm $\times$ 400 mm. The ghosts are located at a distance of ± 70.3 mm and ± 155.2 mm from the correct target, where the experimental locations satisfy the exact theoretical result. In Fig. 15c, the images from the 2nd, 4th, and 10th channels are coherently combined with properly chosen w gains to cancel the first two ghost targets. Fig. 15d shows the image obtained by combining the spectrum of the 1st, 3rd, 9th, 10th, and 12th channels with properly chosen w gains such that all four ghosts are canceled.

Finally, two additional experiments are performed to demonstrate the capability of the prototyped system in real-world security screening scenarios. In both experiments, the SAR aperture size is about 400 mm $\times$ 400 mm. The spatial sampling intervals are selected as $\Delta_x \approx 0.98$ mm and $\Delta_y = 7.59$ mm. The eight virtual channels (1st to 4th and 9th to 12th) are used with their properly chosen w complex gains. For both scenarios, the lateral resolution achieved is about 1.6 mm.

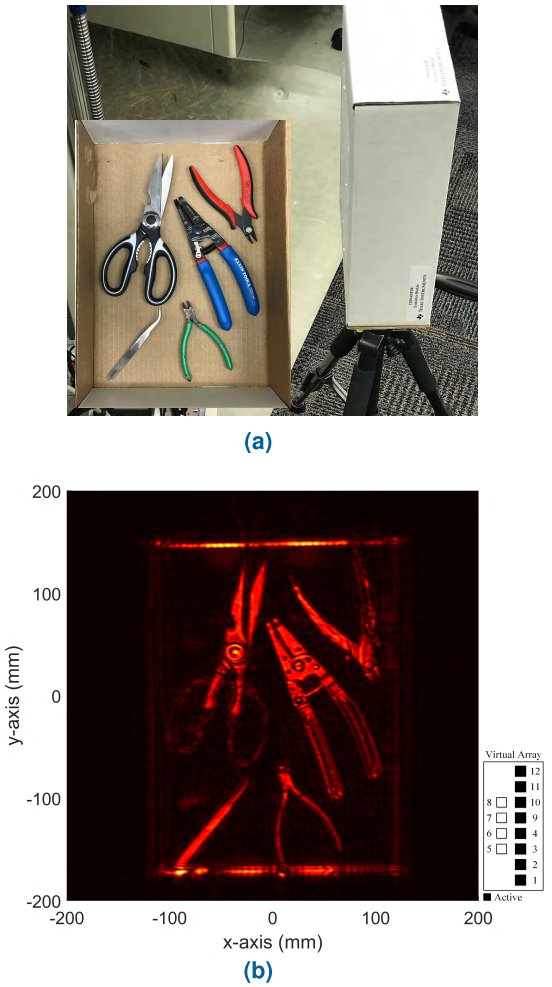

FIGURE 16. Imaging scenario with multiple objects concealed in a cardboard box: (a) optical image, and (b) reconstructed image from eight channels combined using properly chosen w gains.

The imaging scenario in Fig. 16a shows multiple objects (two different wire cutters, a pair of scissors, a wire stripper,

and a pair of tweezers) concealed in a cardboard box. Fig. 16b shows the reconstructed image focused at $z_0 = 270$ mm. All the objects are clearly visible without spatial aliasing.

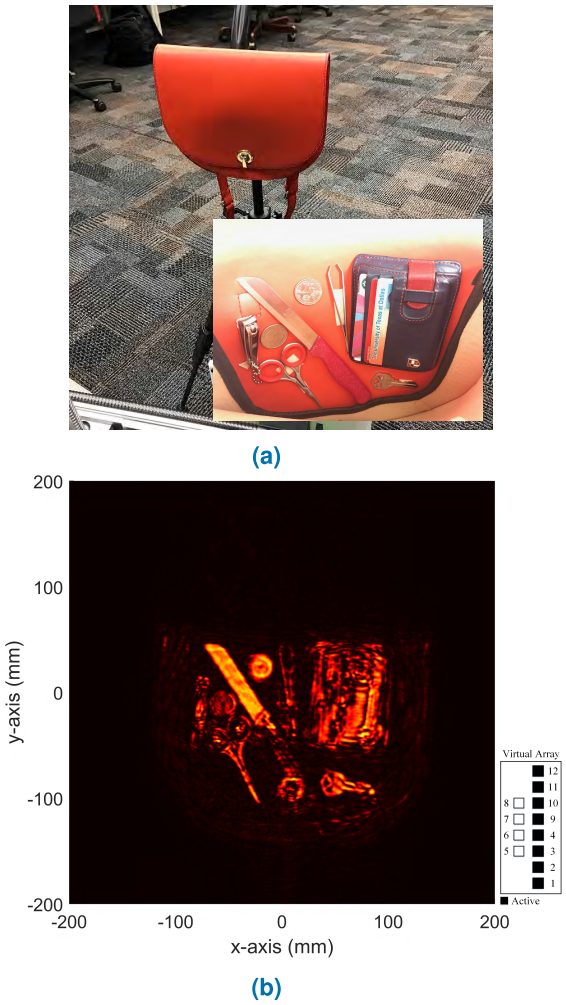

FIGURE 17. Imaging scenario with small items concealed in a leather bag: (a) optical image, and (b) reconstructed image from eight channels combined using properly chosen w gains.

Fig. 17a shows the final imaging scenario for a security screening application. Smaller objects (a pair of small scissors, two coins, a knife, a nail clipper, a pair of small tweezers, a key, and a leather wallet) are concealed in a leather bag. Fig. 17b shows the reconstructed image focused at $z_0 = 254$ mm. All the objects are clearly identified, even the non-metallic wallet and very small objects such as key and nail cutter.

VIII. CONCLUSION

In this paper, we presented a near-field mmWave imaging system utilizing 2-D MIMO array in SAR configuration. We proposed and experimentally verified a computationally efficient novel image reconstruction algorithm based on sparsely sampled aperture data. We analyzed the effect of sparse sampling both on wavenumber spectrum and spatial domains. We involved the calibration method for MIMO array, as well as the complete signal processing chain necessary for the image formation. We investigated the design considerations including the system's bandwidth, spatial sampling criteria, and image resolution. We built a mmWave imaging prototype using commercially available MIMO sensors to validate the proposed image reconstruction method with measurements. We characterized the system performance by the evaluation of PSF, simulations, and real images. The results show that the prototyped system is able to achieve high image quality with a significantly reduced number of antenna elements, thus making the system more affordable and less complex.

APPENDIX A
FOURIER TRANSFORM DEFINITIONS

The 2-D spatial Fourier transform and its inverse are defined by

$$\begin{aligned} S(k_x, k_y) &= \iint s(x, y) e^{-j(k_x x + k_y y)}\, dx\, dy \\ &= \mathrm{FT}_{2D}\big[s(x, y)\big], \end{aligned} \tag{70}$$

$$\begin{aligned} s(x, y) &= \frac{1}{(2\pi)^2} \iint S(k_x, k_y) e^{j(k_x x + k_y y)}\, dk_x\, dk_y \\ &= \mathrm{IFT}_{2D}\big[S(k_x, k_y)\big]. \end{aligned} \tag{71}$$

If the function is shifted in the spatial domain, there is a corresponding phase shift in the Fourier domain:

$$\mathrm{FT}_{2D}\big[s(x - x_0, y - y_0)\big] = e^{-j(k_x x_0 + k_y y_0)} S(k_x, k_y). \tag{72}$$

If the function is shifted in the Fourier domain, there is a corresponding phase shift in the spatial domain:

$$\mathrm{IFT}_{2D}\big[S(k_x - k_0^x, k_y - k_0^y)\big] = e^{j(k_0^x x + k_0^y y)} s(x, y). \tag{73}$$

The 2-D spatial Fourier transform of a 2-D spatial impulse train is given by

$$\begin{aligned} &\mathrm{FT}_{2D}\left[\sum_{p\in\mathbb{Z}}\sum_{q\in\mathbb{Z}} \delta(x - p\Delta_x, y - q\Delta_y)\right] \\ &\qquad = \frac{(2\pi)^2}{\Delta_x \Delta_y} \sum_{m\in\mathbb{Z}}\sum_{n\in\mathbb{Z}} \delta(k_x - m k_x^s, k_y - n k_y^s), \end{aligned} \tag{74}$$

where k_x^s and k_y^s are given in (34).

Multiplication in the spatial domain corresponds to a convolution in the Fourier domain:

$$\mathrm{FT}_{2D}\big[s_1(x, y) s_2(x, y)\big] = \frac{1}{(2\pi)^2} S_1(k_x, k_y) \circledast S_2(k_x, k_y). \tag{75}$$

Differentiation in the spatial domain yields

$$\begin{aligned} \mathrm{FT}_{2D}\left[\frac{\partial s(x, y)}{\partial x}\right] &= j k_x S(k_x, k_y), \\ \mathrm{FT}_{2D}\left[\frac{\partial s(x, y)}{\partial y}\right] &= j k_y S(k_x, k_y). \end{aligned} \tag{76}$$

APPENDIX B
THE METHOD OF STATIONARY PHASE

The method of stationary phase (MSP) provides an analytical solution for integrands, which have a wide phase variation and an envelope of $g(x, y)$, as [39], [40]

$$\iint g(x,y)e^{j\phi(x,y)}\,dx\,dy \approx \frac{j2\pi}{\sqrt{\phi_{xx}\phi_{yy}-\phi_{xy}^2}} \times g(x_0,y_0)e^{j\phi(x_0,y_0)}, \quad (77)$$

where $\phi(x, y)$ is the phase of the exponential that is assumed to be twice-continuously differentiable. A small neighborhood near the points, where the two first derivatives of $\phi(x, y)$ vanish, gives the major contribution to the integral in (77). These points are known as points of stationary phase, where the phase $\phi(x, y)$ takes an extreme value as

$$\left.\frac{\partial\phi(x,y)}{\partial x}\right|_{(x=x_0,y=y_0)} = 0, \qquad \left.\frac{\partial\phi(x,y)}{\partial y}\right|_{(x=x_0,y=y_0)} = 0. \quad (78)$$

In (77), ϕ_{xx}, ϕ_{yy}, and ϕ_{xy} denote the second partial derivatives of $\phi(x, y)$ evaluated at the stationary points. It is assumed that $\phi_{xx}\phi_{yy} - \phi_{xy}^2 \neq 0$. The derivation of (77) is already given in previous studies for single variable [41] or without an envelope $g(x, y)$ factor [21]. Here, the exact analytical solution is given to evaluate the 2-D Fourier transform of spherical wave formula in (19) asymptotically by using MSP.

Substituting (8) into (19), the spherical wave formula becomes

$$\frac{e^{j2kR}}{R} = \frac{e^{j2k\sqrt{(x-x')^2+(y-y')^2+z_0^2}}}{\sqrt{(x-x')^2+(y-y')^2+z_0^2}}. \quad (79)$$

Using the Fourier transform definitions in Appendix A, the 2-D Fourier transform of (79) is evaluated as

$$\mathrm{FT}_{2D}\left[\frac{e^{j2kR}}{R}\right] = e^{-j(k_x x'+k_y y')} \times \iint \frac{e^{j2k\sqrt{x^2+y^2+z_0^2}}}{\sqrt{x^2+y^2+z_0^2}} \times e^{-j(k_x x+k_y y)}\,dx\,dy. \quad (80)$$

The double integral above can be solved analytically using MSP in (77). Let us define the phase and the envelope terms in (80) as

$$\phi(x,y) = 2k\sqrt{x^2+y^2+z_0^2} - k_x x - k_y y, \quad (81)$$

$$g(x,y) = 1/\sqrt{x^2+y^2+z_0^2}. \quad (82)$$

The first derivatives of (81)

$$\phi_x(x,y) = \frac{\partial\phi(x,y)}{\partial x} = \frac{2kx}{\sqrt{x^2+y^2+z_0^2}} - k_x,$$

$$\phi_y(x,y) = \frac{\partial\phi(x,y)}{\partial y} = \frac{2ky}{\sqrt{x^2+y^2+z_0^2}} - k_y, \quad (83)$$

give the stationary points in (78) as

$$x_0 = \frac{k_x z_0}{\sqrt{4k^2-k_x^2-k_y^2}}, \qquad y_0 = \frac{k_y z_0}{\sqrt{4k^2-k_x^2-k_y^2}}. \quad (84)$$

In order to ensure the asymptotic expansion provided by the MSP valid, the coordinates must be both real such that the frequency wavenumber must satisfy the following inequality

$$k_x^2 + k_y^2 \leq 4k^2. \quad (85)$$

Substituting (84) into (81) and (82), the phase and the envelope evaluated at the stationary points yield

$$\phi(x_0,y_0) = \sqrt{4k^2-k_x^2-k_y^2}\,z_0, \quad (86)$$

$$g(x_0,y_0) = \frac{\sqrt{4k^2-k_x^2-k_y^2}}{2kz_0}, \quad (87)$$

respectively. Similarly, the second partial derivatives of the phase evaluated at the stationary points are calculated as

$$\phi_{xx} = \frac{\sqrt{4k^2-k_x^2-k_y^2}(4k^2-k_x^2)}{4k^2 z_0},$$

$$\phi_{yy} = \frac{\sqrt{4k^2-k_x^2-k_y^2}(4k^2-k_y^2)}{4k^2 z_0},$$

$$\phi_{xy} = -\frac{\sqrt{4k^2-k_x^2-k_y^2}\,k_x k_y}{4k^2 z_0}, \quad (88)$$

which yields the denominator in (77) as

$$\sqrt{\phi_{xx}\phi_{yy}-\phi_{xy}^2} = \frac{(4k^2-k_x^2-k_y^2)}{2kz_0}. \quad (89)$$

Substituting (86), (87) and (89) into (77), the resulting 2-D Fourier transform expression in (80) is expressed as

$$\mathrm{FT}_{2D}\left[\frac{e^{j2kR}}{R}\right] = \frac{j2\pi}{k_z}e^{-j(k_x x'+k_y y'-k_z z_0)}, \quad (90)$$

where the spatial wavenumber k_z is given in (20). Finally, from the 2-D inverse Fourier transform operation in Appendix A, the spherical wave formula is computed as

$$\frac{e^{j2kR}}{R} = \frac{j}{2\pi}\iint \frac{e^{j(k_x(x-x')+k_y(y-y')+k_z z_0)}}{k_z}\,dk_x\,dk_y. \quad (91)$$

APPENDIX C
MULTIVARIATE TAYLOR SERIES EXPANSION

Let f be an infinitely differentiable real or complex-valued function in some open neighborhood around $(x, y) = (x_0, y_0)$. Let $\mathbf{x} = [x\ y]$ and let $\mathbf{x_0} = [x_0\ y_0]$. With this vector notation, the Taylor series of $f(\mathbf{x})$ in a neighborhood of $\mathbf{x_0}$ is

$$f(\mathbf{x}) = f(\mathbf{x_0}) + [(\mathbf{x}-\mathbf{x_0})\cdot\nabla\mathbf{f}(\mathbf{x_0})] + \frac{1}{2!}[(\mathbf{x}-\mathbf{x_0})\cdot\mathbf{H}(\mathbf{x_0})\cdot(\mathbf{x}-\mathbf{x_0})^T] + \ldots, \quad (92)$$

where $\nabla\mathbf{f}$ is the vector of first derivatives

$$\nabla\mathbf{f}(x,y)=\begin{bmatrix}f_x(x,y)\\ f_y(x,y)\end{bmatrix}, \tag{93}$$

and $\mathbf{H}$ is the matrix of second derivatives, called the Hessian matrix

$$\mathbf{H}(x,y)=\begin{bmatrix}f_{xx}(x,y) & f_{xy}(x,y)\\ f_{yx}(x,y) & f_{yy}(x,y)\end{bmatrix}. \tag{94}$$

A. TAYLOR SERIES EXPANSION OF THE ROUND-TRIP DISTANCE

Substituting the transmitter and receiver locations in (6) into (5), the total round-trip distance associated with the uth transmitter element at $(x_u, y_u, 0)$ and the vth receiver element at $(x_v, y_v, 0)$ to a point scatterer at (x', y', z_0) becomes

$$R_\ell=\sqrt{(x+d_\ell^x/2-x')^2+(y+d_\ell^y/2-y')^2+z_0^2}+\sqrt{(x-d_\ell^x/2-x')^2+(y-d_\ell^y/2-y')^2+z_0^2}. \tag{95}$$

Evaluating the first derivatives of (95) at $(d_\ell^x=0, d_\ell^y=0)$ yields

$$\left.\frac{\partial R_\ell}{\partial d_\ell^x}\right|_{(d_\ell^x=0,d_\ell^y=0)}=\left.\frac{\partial R_\ell}{\partial d_\ell^y}\right|_{(d_\ell^x=0,d_\ell^y=0)}=0. \tag{96}$$

Similarly, the second partial derivatives of (95) evaluated at $(d_\ell^x=0, d_\ell^y=0)$ yields

$$\begin{aligned}\left.\frac{\partial^2 R_\ell}{\partial (d_\ell^x)^2}\right|_{(d_\ell^x=0,d_\ell^y=0)}&=\frac{1}{2R}\left[1-\frac{(x-x')^2}{R^2}\right],\\ \left.\frac{\partial^2 R_\ell}{\partial (d_\ell^y)^2}\right|_{(d_\ell^x=0,d_\ell^y=0)}&=\frac{1}{2R}\left[1-\frac{(y-y')^2}{R^2}\right],\\ \left.\frac{\partial^2 R_\ell}{\partial d_\ell^x\partial d_\ell^y}\right|_{(d_\ell^x=0,d_\ell^y=0)}&=-\frac{(x-x')(y-y')}{2R^3},\end{aligned} \tag{97}$$

where R is given in (8). Substituting (96) and (97) into (92), quadratic approximation of R_ℓ is given by

$$R_\ell\approx 2R+\frac{(d_\ell^x)^2+(d_\ell^y)^2}{4R}-\frac{((x-x')d_\ell^x+(y-y')d_\ell^y)^2}{4R^3}. \tag{98}$$

B. TAYLOR SERIES EXPANSION OF THE GHOST IMAGE SPECTRUM COMPONENTS

Evaluating the amplitude factor (41) at $(k_x=mk_x^s, k_y=nk_y^s)$ gives

$$\vartheta(mk_x^s, nk_y^s)=\frac{G_{mn}}{2k}, \tag{99}$$

where G_{mn} is given in (44). Similarly, the first derivatives of (41) evaluated at $(k_x=mk_x^s, k_y=nk_y^s)$ yields

$$\left.\frac{\partial\vartheta(k_x,k_y)}{\partial k_x}\right|_{(k_x=mk_x^s,k_y=nk_y^s)}=-\frac{mk_x^s}{2kG_{mn}},$$

$$\left.\frac{\partial\vartheta(k_x,k_y)}{\partial k_y}\right|_{(k_x=mk_x^s,k_y=nk_y^s)}=-\frac{nk_y^s}{2kG_{mn}}. \tag{100}$$

Substituting (99) and (100) into (92), linear approximation of $\vartheta(k_x, k_y)$ becomes

$$\vartheta(k_x,k_y)\approx\frac{G_{mn}}{2k}-\frac{mk_x^s}{2kG_{mn}}(k_x-mk_x^s)-\frac{nk_y^s}{2kG_{mn}}(k_y-nk_y^s), \tag{101}$$

which can be further simplified as

$$\vartheta(k_x,k_y)\approx\frac{2k}{G_{mn}}-\frac{mk_x^s}{2kG_{mn}}k_x-\frac{nk_y^s}{2kG_{mn}}k_y. \tag{102}$$

Evaluating the phase factor in (42) at $(k_x=mk_x^s, k_y=nk_y^s)$ results in

$$\varphi(mk_x^s, nk_y^s)=(2k-G_{mn})z_0. \tag{103}$$

Similarly, the first derivatives of (42) evaluated at $(k_x=mk_x^s, k_y=nk_y^s)$ yields

$$\begin{aligned}\left.\frac{\partial\varphi(k_x,k_y)}{\partial k_x}\right|_{(k_x=mk_x^s,k_y=nk_y^s)}&=\frac{mk_x^s z_0}{G_{mn}},\\ \left.\frac{\partial\varphi(k_x,k_y)}{\partial k_y}\right|_{(k_x=mk_x^s,k_y=nk_y^s)}&=\frac{nk_y^s z_0}{G_{mn}}.\end{aligned} \tag{104}$$

Substituting (103) and (104) into (92), linear approximation of $\varphi(k_x, k_y)$ becomes

$$\varphi(k_x,k_y)\approx(2k-G_{mn})z_0+\frac{mk_x^s z_0}{G_{mn}}(k_x-mk_x^s)+\frac{nk_y^s z_0}{G_{mn}}(k_y-nk_y^s), \tag{105}$$

which can be further simplified as

$$\varphi(k_x,k_y)\approx 2kz_0\left(1-\frac{2k}{G_{mn}}\right)+\frac{mk_x^s z_0}{G_{mn}}k_x+\frac{nk_y^s z_0}{G_{mn}}k_y. \tag{106}$$

REFERENCES

[1] L. Chao, M. N. Afsar, and K. A. Korolev, "Millimeter wave dielectric spectroscopy and breast cancer imaging," in *Proc. 7th Eur. Microw. Integr. Circuit Conf.*, Amsterdam, The Netherlands, Oct. 2012, pp. 572–575.
[2] S. D. Meo *et al.*, "High-resolution mm-Wave imaging techniques and systems for breast cancer detection," in *IEEE MTT-S Int. Microw. Symp. Dig.*, Pavia, Italy, Sep. 2017, pp. 1–3.
[3] Y. Gao and R. Zoughi, "Millimeter wave reflectometry and imaging for noninvasive diagnosis of skin burn injuries," *IEEE Trans. Instrum. Meas.*, vol. 66, no. 1, pp. 77–84, Jan. 2017.
[4] D. M. Sheen, D. L. McMakin, and T. E. Hall, "Three-dimensional millimeter-wave imaging for concealed weapon detection," *IEEE Trans. Microw. Theory Techn.*, vol. 49, no. 9, pp. 1581–1592, Sep. 2001.
[5] X. Zhuge and A. G. Yarovoy, "A sparse aperture MIMO-SAR-based UWB imaging system for concealed weapon detection," *IEEE Trans. Geosci. Remote Sens.*, vol. 49, no. 1, pp. 509–518, Jan. 2011.
[6] S. S. Ahmed, A. Schiessl, F. Gumbmann, M. Tiebout, S. Methfessel, and L.-P. Schmidt, "Advanced microwave imaging," *IEEE Microw. Mag.*, vol. 13, no. 6, pp. 26–43, Sep./Oct. 2012.
[7] R. Appleby and R. N. Anderton, "Millimeter-wave and submillimeter-wave imaging for security and surveillance," *Proc. IEEE*, vol. 95, no. 8, pp. 1683–1690, Aug. 2007.
[8] J. L. Fernandes, J. R. Tedeschi, D. M. Sheen, and D. L. McMakin, "Three-dimensional millimeter-wave imaging for concealed threat detection in shoes," *Proc. SPIE*, vol. 8715, May 2013, Art. no. 87150C.

[9] M. E. Yanik and M. Torlak, "Near-field 2-D SAR imaging by millimeter-wave radar for concealed item detection," in *Proc. IEEE Radio Wireless Symp.*, Orlando, FL, USA, Jan. 2019.
[10] S. Kharkovsky, J. T. Case, M. A. Abou-Khousa, R. Zoughi, and F. L. Hepburn, "Millimeter-wave detection of localized anomalies in the space shuttle external fuel tank insulating foam," *IEEE Trans. Instrum. Meas.*, vol. 55, no. 4, pp. 1250–1257, Aug. 2006.
[11] K. Ramasubramanian and J. Singh, "AWR1443 single-chip radar: For diverse proximity-sensing applications," Texas Instrum., Dallas, TX, USA, Tech. Rep. SPYY008, May 2017.
[12] D. W. Bliss and K. W. Forsythe, "Multiple-input multiple-output (MIMO) radar and imaging: degrees of freedom and resolution," in *Proc. 37th Asilomar Conf. Signals, Syst. Comput.*, Pacific Grove, CA, USA, vol. 1, Nov. 2003, pp. 54–59.
[13] J. Li and P. Stoica, *MIMO Radar Signal Processing*. Hoboken, NJ, USA: Wiley, 2009.
[14] J. Li and P. Stoica, "MIMO radar with colocated antennas," *IEEE Signal Process. Mag.*, vol. 24, no. 5, pp. 106–114, Sep. 2007.
[15] S. S. Ahmed, A. Schiessl, and L.-P. Schmidt, "A novel fully electronic active real-time imager based on a planar multistatic sparse array," *IEEE Trans. Microw. Theory Techn.*, vol. 59, no. 12, pp. 3567–3576, Dec. 2011.
[16] W. F. Moulder *et al.*, "Development of a high-throughput microwave imaging system for concealed weapons detection," in *Proc. IEEE Int. Symp. Phased Array Syst. Technol.*, Waltham, MA, USA, Oct. 2016, pp. 1–6.
[17] M. A. Richards, "A beginner's guide to interferometric SAR concepts and signal processing [AESS tutorial IV]," *IEEE Aerosp. Electron. Syst. Mag.*, vol. 22, no. 9, pp. 5–29, Sep. 2007.
[18] G. Franceschetti and R. Lanari, *Synthetic Aperture Radar Processing*. New York, NY, USA: CRC Press, 1999.
[19] R. Zhu, J. Zhou, G. Jiang, and Q. Fu, "Range migration algorithm for near-field MIMO-SAR imaging," *IEEE Geosci. Remote Sens. Lett.*, vol. 14, no. 12, pp. 2280–2284, Dec. 2017.
[20] M. Soumekh, "Wide-bandwidth continuous-wave monostatic/bistatic synthetic aperture radar imaging," in *Proc. Int. Conf. Image Process.*, Chicago, IL, USA, vol. 3, Oct. 1998, pp. 361–365.
[21] J. M. Lopez-Sanchez and J. Fortuny-Guasch, "3-D radar imaging using range migration techniques," *IEEE Trans. Antennas Propag.*, vol. 48, no. 5, pp. 728–737, May 2000.
[22] M. E. Yanik and M. Torlak, "Millimeter-wave near-field imaging with two-dimensional SAR data," in *Proc. SRC Techcon*, Austin, TX, USA, Sep. 2018.
[23] D. Sheen, D. McMakin, and T. Hall, "Near-field three-dimensional radar imaging techniques and applications," *Appl. Opt.*, vol. 49, no. 19, pp. E83–E93, Jul. 2010.
[24] J. Fortuny-Guasch and J. M. Lopez-Sanchez, "Extension of the 3-D range migration algorithm to cylindrical and spherical scanning geometries," *IEEE Trans. Antennas Propag.*, vol. 49, no. 10, pp. 1434–1444, Oct. 2001.
[25] X. Zhuge and A. G. Yarovoy, "Three-dimensional near-field MIMO array imaging using range migration techniques," *IEEE Trans. Image Process.*, vol. 21, no. 6, pp. 3026–3033, Jun. 2012.
[26] Y. Álvarez, Y. Rodriguez-Vaqueiro, B. Gonzalez-Valdes, F. Las-Heras, and A. García-Pino, "Fourier-based imaging for subsampled multistatic arrays," *IEEE Trans. Antennas Propag.*, vol. 64, no. 6, pp. 2557–2562, Jun. 2016.
[27] B. P. Ng, J. P. Lie, M. H. Er, and A. Feng, "A practical simple geometry and gain/phase calibration technique for antenna array processing," *IEEE Trans. Antennas Propag.*, vol. 57, no. 7, pp. 1963–1972, Jul. 2009.
[28] C. M. Schmid, C. Pfeffer, R. Feger, and A. Stelzer, "An FMCW MIMO radar calibration and mutual coupling compensation approach," in *Proc. Eur. Radar Conf.*, Nuremberg, Germany, Oct. 2013, pp. 13–16.
[29] J. H. G. Ender and J. Klare, "System architectures and algorithms for radar imaging by MIMO-SAR," in *Proc. IEEE Radar Conf.*, Pasadena, CA, USA, May 2009, pp. 1–6.
[30] Y. Qi, Y. Wang, W. Tan, and W. Hong, "Application of sparse array and MIMO in near-range microwave imaging," *Proc. SPIE*, vol. 8179, Oct. 2011, Art. no. 81790X.
[31] L. Qiao, Y. Wang, Z. Zhao, and Z. Chen, "Exact reconstruction for near-field three-dimensional planar millimeter-wave holographic imaging," *J. Infr., Millim., THz. Waves*, vol. 36, no. 12, pp. 1221–1236, Dec. 2015.
[32] A. Meta, P. Hoogeboom, and L. P. Ligthart, "Signal processing for FMCW SAR," *IEEE Trans. Geosci. Remote Sens.*, vol. 45, no. 11, pp. 3519–3532, Nov. 2007.
[33] G. Wang, J.-M. Muñoz-Ferreras, C. Gu, C. Li, and R. Gómez-García, "Application of linear-frequency-modulated continuous-wave (LFMCW) radars for tracking of vital signs," *IEEE Trans. Microw. Theory Techn.*, vol. 62, no. 6, pp. 1387–1399, Jun. 2014.
[34] S. D. Silverstein and Y. Zheng, "Near-field inverse coherent imaging problems: Solutions, simulations and applications," in *Proc. 37th Asilomar Conf. Signals, Syst. Comput.*, Pacific Grove, CA, USA, vol. 1, Nov. 2003, pp. 1193–1197.
[35] H. Weyl, "Ausbreitung elektromagnetischer wellen über einem ebenen leiter," *Ann. Phys*, vol. 365, no. 21, pp. 481–500, 1919.
[36] L. M. Brekhovskikh and O. Godin, *Acoustics of Layered Media II: Point Sources and Bounded Beams*. New York, NY, USA: Springer, 1999.
[37] M. E. Yanik and M. Torlak, "Geolocalization via tracking of wideband radio astronomical sources in the presence of radio frequency interference," in *Proc. IEEE/ION Position, Location Navigat. Symp.*, Monterey, CA, USA, Apr. 2018, pp. 1234–1238.
[38] D. C. Rife and R. R. Boorstyn, "Single tone parameter estimation from discrete-time observations," *IEEE Trans. Inf. Theory*, vol. IT-20, no. 5, pp. 591–598, Sep. 1974.
[39] C. E. Cook and M. Bernfeld, *Radar Signals: An Introduction to Theory and Application* (Electrical Science). New York, NY, USA, 1967.
[40] A. Papoulis, *Systems and Transforms with Applications in Optics*. New York, NY, USA: McGraw-Hill, 1968.
[41] P. T. Gough and D. W. Hawkins, "Imaging algorithms for a strip-map synthetic aperture sonar: Minimizing the effects of aperture errors and aperture undersampling," *IEEE J. Ocean. Eng.*, vol. 22, no. 1, pp. 27–39, Jan. 1997.

MUHAMMET EMIN YANIK (S'17) received the B.S. and M.S. degrees in electrical and electronics engineering from Hacettepe University, in 2007 and 2010, respectively. He is currently pursuing the Ph.D. degree in electrical engineering with The University of Texas at Dallas. He was with Aselsan, Ankara, Turkey, from 2007 to 2016, where he was involved in real-time embedded system development for safety-critical avionics applications. His current research interests include millimeter-wave radars, ultrawideband radar imaging systems, real-time embedded system development, phased array signal processing, and interference mitigation in radio telescopes. He was a recipient of the Tubitak Graduate Fellowship, from 2007 to 2009, the Turkcell Academy Fellowship, from 2012 to 2013, and the Best Poster Award at TxACE and Analog/Mixed Signal Circuits Annual Review, in 2018.

MURAT TORLAK (SM'04) received the M.S. and Ph.D. degrees in electrical engineering from The University of Texas at Austin, in 1995 and 1999, respectively. Since 1999, he has been with the Department of Electrical Engineering, The University of Texas, where he has been promoted to the rank of Full Professor. He spent the summers of 1997 and 1998 in Cwill Telecommunications, Inc., Austin, TX, USA, where he participated in the design of a smart antenna wireless local loop system and directed research and development efforts toward standardization of TD-SCDMA for the International Telecommunication Union. He was a Visiting Scholar with the University of California at Berkeley, in 2008. He has been an active contributor in the areas of smart antennas and multiuser detection. His current research interests include millimeter-wave automotive radars, millimeter-wave imaging systems, cognitive radios, and interference mitigation in radio telescopes. He was the Program Chair of the IEEE Signal Processing Society Dallas Chapter, from 2003 to 2005. He has served on the Technical Program Committees of several IEEE conferences. He was the General Chair of the Symposium on Millimeter Wave Imaging and Communications in the 2013 IEEE GlobalSIP Conference. He served as an Associate Editor for the IEEE TRANSACTIONS ON WIRELESS COMMUNICATIONS, from 2008 to 2013.